Appendix 5.2-A

Analytical Modeling of Alternative Wind Farm Sites - Existing Conditions

Analytical Modeling of Alternative Wind Farm Sites
Existing Conditions

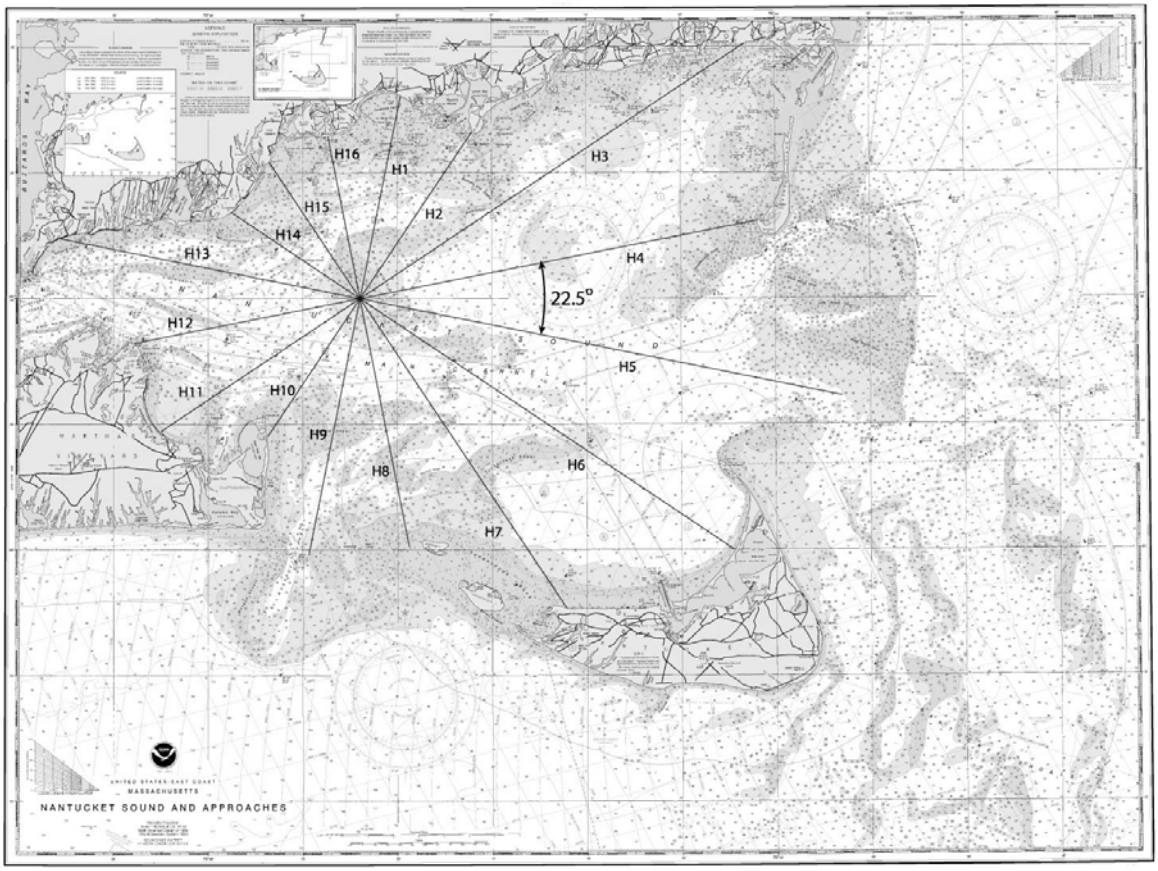

Woods Hole Group
81 Technology Park Drive
East Falmouth MA 02536

March 2004

Analytical Modeling of Alternative Wind Farm Sites
Existing Conditions

March 2004

Prepared for:
Cape Wind Associates, LLC
75 Arlington Street, Suite 704
Boston, MA 02116

Prepared by:
Woods Hole Group
81 Technology Park Drive
East Falmouth MA 02536
(508) 540-8080

Table of Contents

LIST OF FIGURES

LIST OF TABLES

1.0 Introduction

1.0 INTRODUCTION

This report presents the results of a modeling investigation, designed to provide information that will help characterize the regional and local processes surrounding alternative wind farm locations in Nantucket Sound, MA. A concise summary of the data, modeling, and conclusions is provided in Section 4. The alternative sites evaluated included Horseshoe Shoal, Tuckernuck Shoal, and Handkerchief Shoal (Figure 1-1). Coastal processes evaluated included winds, waves, tidal and wind-driven currents, and sediment transport. These processes were evaluated based on existing data, current measurements conducted for this investigation, and analytical models applied to the specific sites.

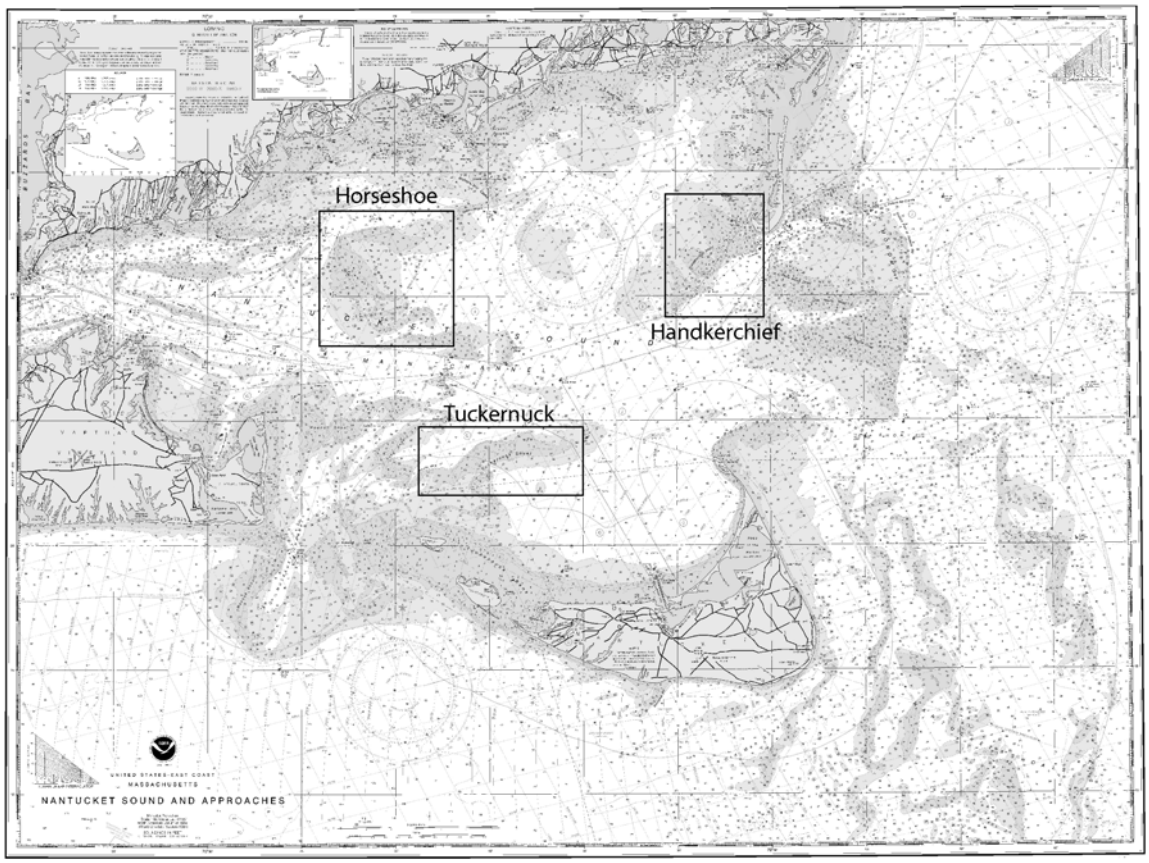

Figure 1-1. Area of investigation including three alternative wind farm locations

This work was performed under contract to Cape Wind. It is our understanding that Cape Wind is seeking this information in a proactive manner to:

- Prepare an Environmental Impact Statement
- Gain a better understanding of existing conditions in the Sound;
- Help select an appropriate site; and
- Prepare for later phases of the project (i.e., impact assessment, designing, etc.)

The analytical modeling approach presented here, which is based on existing data, provides the first level of information required to understand existing conditions.

The results of this investigation are presented in the three following sections of this report:

- Section 2.0 Data Collection – Describes existing data sets that were compiled for this analysis, as well as current measurements that were collected for this investigation at the alternative sites.
- Section 3.0 Analytical Modeling – Presents the methodology and results of the wave, current, and sediment transport modeling.
- Section 4.0 Summary and Conclusions – Summarizes the outcome of the investigation, how the results may be applied to the wind farm project, and conclusions.

2.0 Data Collection

2.0 DATA COLLECTION

Existing data and new data were collected to support this investigation. The data type, extent, and source, as well as a summary of the data are discussed below.

2.1 Existing Data and Information

The following existing data and information were compiled to support the investigation:

2.1.1 Winds

Wind data were collected from the National Climatic Data Center (NCDC-www.ncdc.noaa.gov) at Otis Air Force Base, Hyannis Airport, and Nantucket Airport. The data sets spanned from the late 1940's to present at Otis, 1973-2001 at Hyannis, and 1986-2001 at Nantucket. Hourly average wind speed and direction were obtained along with wind gust information. Wind data provided input information for the wind wave generation model described in Section 3.0. Winds at the three local airports were compared to gain knowledge of the spatial variability of winds in this region, and to select the appropriate wind data source for the wave modeling.

Figures 2-1 through 2-3 illustrate wind roses for the hourly average wind data obtained for the three airports. These figures show the distribution of wind speed (mph), wind direction from, and frequency of occurrence. The gray-scale indicates the magnitude of wind speed, with darker shading corresponding to higher wind speeds. The circular axis represents the direction of wind approach (coming from) relative to North (0 degrees), and the extending radial lines indicate percent occurrence within each magnitude and directional band. As an example of how to read the plot, Figure 2-1 shows that winds at Otis Air Force Base most commonly blow from the SW (225º), at speeds between 5 and 15 mph. Maximum speeds exceed 25 mph. The figure also shows that winds blow from directions between 180° and 270° (SW) approximately 40 percent of the time.

A comparison of Figures 2-1 through 2-3 shows that winds are relatively similar between the three sites. The westerly and easterly components of the wind at Otis and Hyannis are smaller than at Nantucket, due to the effects of the land mass on reducing the wind speed. As such, the Nantucket winds were selected as most representative of open water conditions within Nantucket Sound, and were used as input to the wind wave generation model. This was also a conservative assumption, in that the highest wind speeds were used, which will produce larger waves as compared to using winds from Otis or Hyannis.

2.1.2 Bathymetry

Water depth, or bathymetry, data were compiled from various sources, including National Oceanographic and Atmospheric Administration (NOAA) Chart 13237, NOAA Geophysical Data System (GEODAS) CD, and from a ESS bathymetry survey conducted by a Cape Wind consultant (ESS) in the vicinity of Horseshoe Shoal. Available data covered almost completely each of the three alternative sites. Data were linearly interpolated to develop a model grid for each of the alternative sites separately, with a grid mesh with 400 ft x 400 ft size cells in both horizontal dimensions (North to South

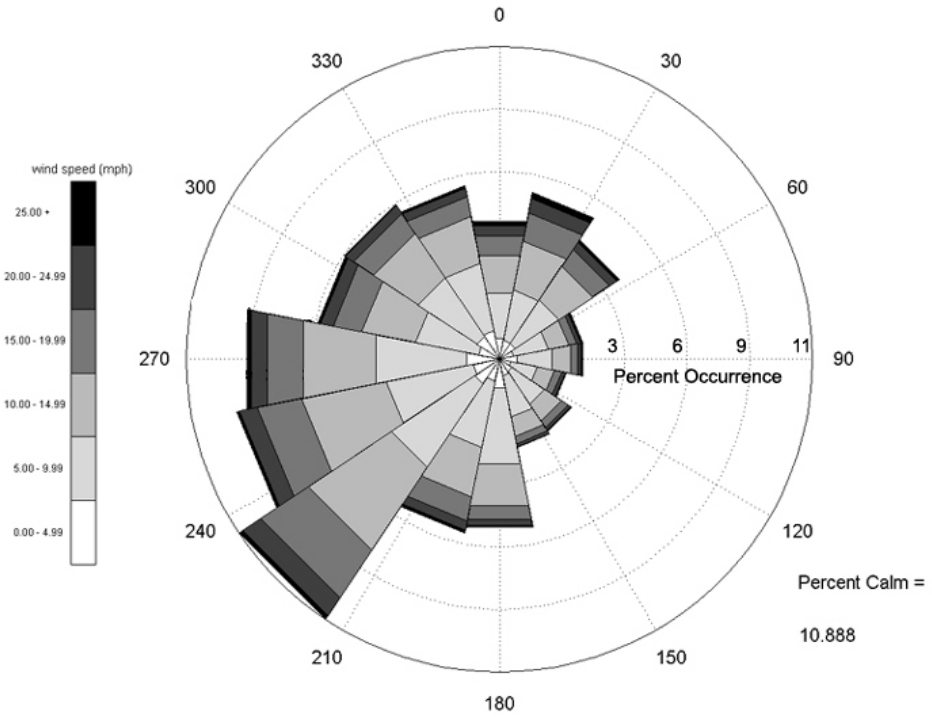

Figure 2-1. Wind rose for Otis Air Force base (late 1940s to present)

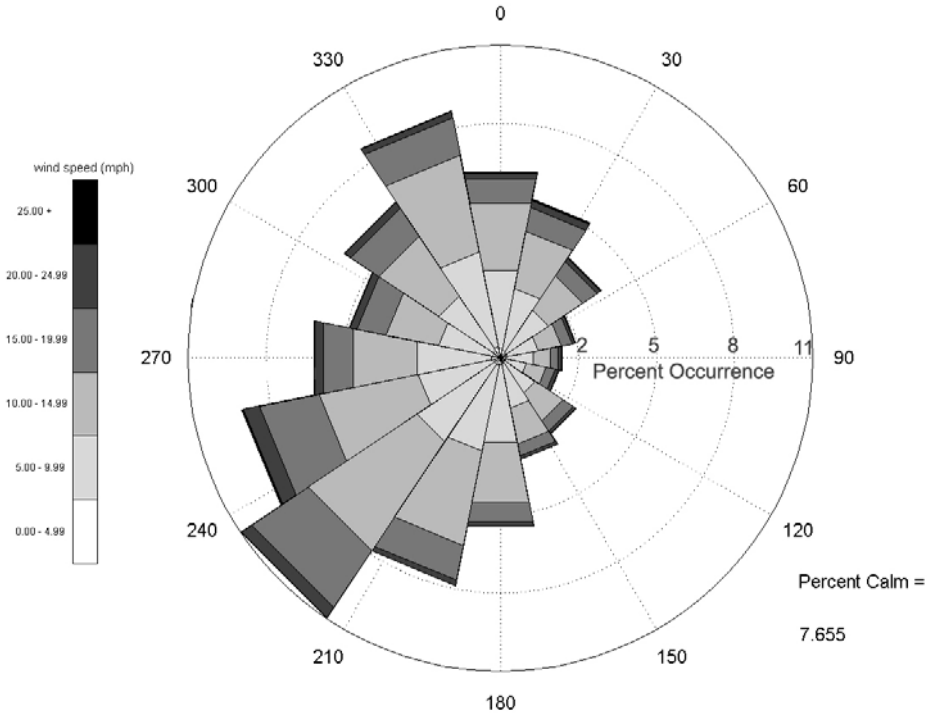

Figure 2-2. Wind rose for Hyannis Airport (1973-2001)

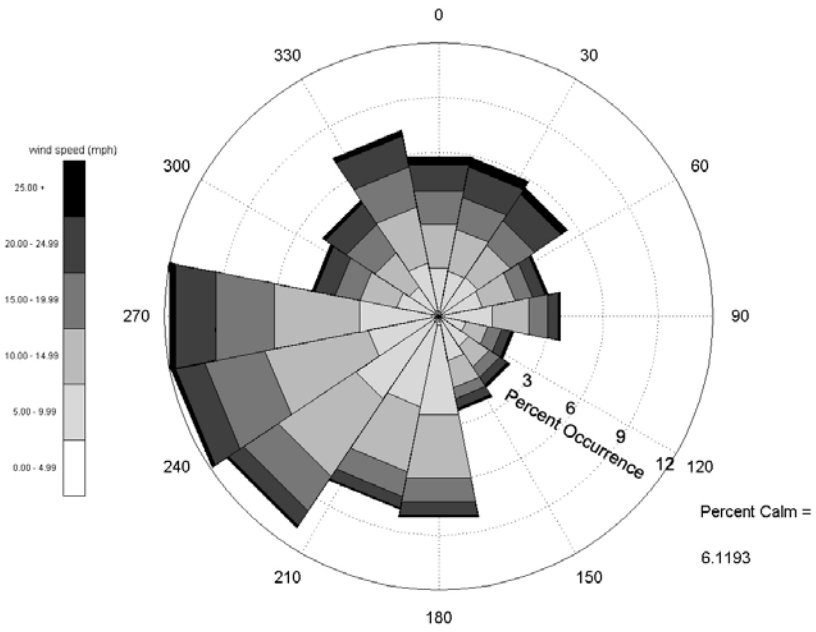

Figure 2-3. Wind rose for Nantucket Airport (1986-2001)

and East to West) for each site. Figures 2-4 through 2-6 illustrate a bathymetry grid for each alternative site. Water depths are in feet relative to mean low water (MLW), corresponding to the color bar. The solid lines represent depth contours. The horizontal coordinate system for the mesh grid system is Massachusetts State Plane Coordinates, Island Zone in feet. The figures show that each alternative site is a shoal with a complex shape, and a range of water depths from less than 10 ft deep to more than 50 ft deep at low tide.

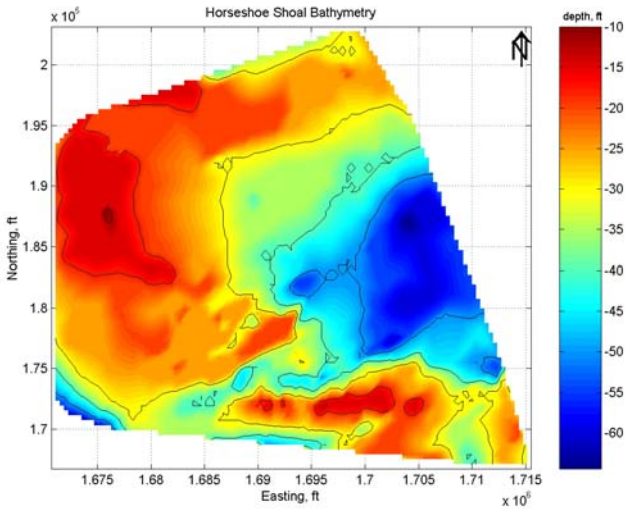

Figure 2-4. Bathymetry at Horseshoe Shoal

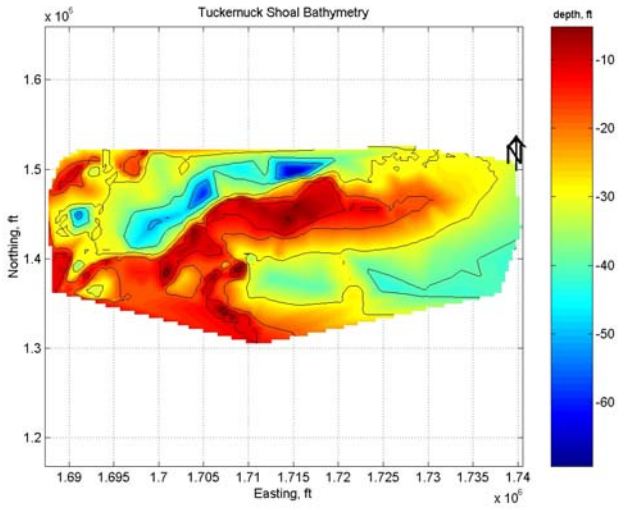

Figure 2-5. Bathymetry at Tuckernuck Shoal

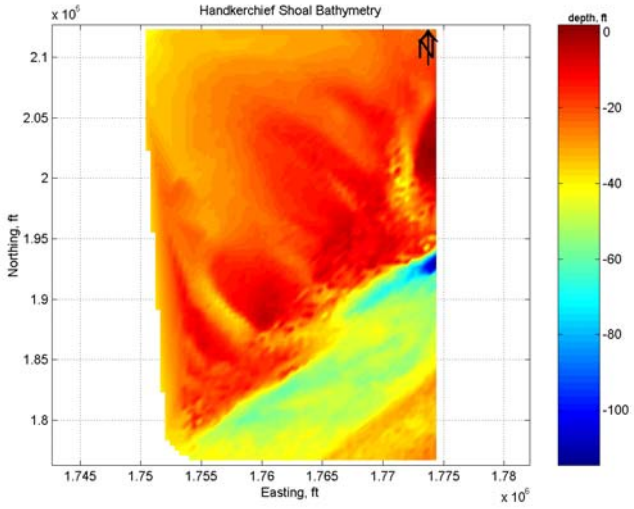

Figure 2-6. Bathymetry at Handkerchief Shoal

2.1.3 Sediment Grain Size

Sediment distribution also was evaluated for the entire Nantucket Sound, based upon median and mean grain size (d_{50}/d_{mean}) compiled by the United States Geological Survey (USGS) (O'Hara and Oldale, 1987) for a number of different locations. The median sizes for each alternative wind farm site are shown in Table 2-1. A constant median sand grain size was assumed for each site.

Table 2-1. Median grain sizes for each alternative site

Location	Median Grain size, mm	
Horseshoe Shoal	0.50	(0.5-0.57)
Tuckernuck Shoal	0.16	(0.1-0.22)
Handkerchief Shoal	0.25	(0.16-0.34)

2.1.4 Offshore Oceanic Wave Conditions

No direct measurements of waves were available at the alternative sites. Waves at the sites are likely composed primarily of waves developed by winds within Nantucket Sound, and secondarily of waves entering the Sound from the Ocean. Wind waves can be modeled based on the wind data presented in 2.1.1, and this modeling is presented in Section 3.1. The basis for evaluating ocean-derived waves at the alternative sites, however, is based upon available data within the Ocean, which are presented in this section. Ocean waves can potentially travel to the Nantucket Sound sites from the east through the opening between Monomoy Island and Nantucket, as well as from the south between Nantucket and Martha's Vineyard. However, due to the wider opening between Monomoy and Nantucket, the direct exposure to the alternative sites, and the prevalence of ocean waves from easterly directions, ocean wave data were used from an area east of the Monomoy/Nantucket Islands. Ocean waves traveling through the narrow gap between Nantucket and Martha's Vineyard were not included in the analysis.

Characteristics of the offshore wave climate were determined by examining records from offshore wave buoys, as well as Wave Information Studies (WIS) performed by the U.S. Army Corps of Engineers (USACE-www.bigfoot.wes.army.mil\w002.html). Offshore wave data were available from offshore buoys east and southeast from Nantucket (NOAA Buoy No. 44003 (40.8N 68.5W), 44008 (40.5N 69.43W), and 44011 (41.06N 66.58W)). Hindcast WIS wave data were available from two sites south of Marthas Vineyard and Nantucket (WIS sites 2089, 2090, and 2091), as well as two sites east of Nantucket and Monomoy Island (WIS sites 2086 and 2087). An examination of these various data sources showed that the best representation of offshore swell waves most likely to propagate toward Nantucket Sound and the alternative areas of interest can be obtained from WIS station 2090 (41.50N 69.75W). Figure 2-7 illustrates a wave rose from this WIS information. The USACE WIS provided 40 years of hindcast significant wave height, peak period and direction for this site between 1956 and 1995. Although there are extensive shoals and only relatively narrow openings between the Sound and the Ocean, which likely prevent significant amounts of Ocean wave energy from entering the Sound, a conservative assumption was made for this analysis that the waves propagate through unchanged.

2.1.5 Tidal Currents in Nantucket Sound

A current survey was conducted for the investigation as discussed in Section 2.2 to support the analytical modeling. Additionally, existing sources of current information were collected. Regular observations of currents in the area have been carried out since the 1840s, and a general pattern of tidal currents in the Nantucket Sound is well known and documented. Navigation charts of the region, as well as the Eldridge tide and pilot

books, contain information on the maximum flood and ebb tides in the main channels and along navigation routes of the region. Information on major harmonic constants is available from NOAA for several reference points as well. For these locations, predictions of tidal currents for any specific time are available from various sources. In this analysis, data were used from a Chart Navigator CD, version 5.0, developed by Maptech Inc., which provides a summary of the available information on tidal currents. The original historical data published by F.J. Haight (Haight, 1938) also were used to develop the representation of existing tidal currents at the alternative sites. The list of stations for which either historical data or current predictions are available and which have been used in this analysis is provided in Table 2-2.

2.2 Current Measurements

Current measurements were collected for this investigation at each of the three alternative wind farm sites. Horseshoe Shoal was surveyed on April 30, 2002. Tuckernuck and Handkerchief Shoals were surveyed on June 3, 2002. Surveys were conducted aboard a 25 ft workboat, equipped with a 1200 kHz Acoustic Doppler Profiler (ADCP) manufactured by RD Instruments. The ADCP was mounted to the vessel in a downward looking configuration, and programmed to collect data in a bottom-tracking mode as the survey vessel traversed the area. Raw current data were collected every five seconds (four pings per ensemble) for 0.5 meter bins throughout the water column (absent the depth below the surface of the instrument), as well as one 0.5 meter bin at the instrument and one at the seafloor. Current data were recorded on to a laptop computer on the survey vessel along with position data from a differential global positioning system (DGPS). Together, the ADCP and DGPS provided a comprehensive data set to characterize currents, and were used in the analytical model discussed in Section 3.0. The current data are presented in Section 3.2.

Survey track lines are shown on Figure 2-8. The Horseshoe Shoal survey data were collected continuously along the track lines as the vessel traversed between points A, B, and C. The triangular survey route was completed three times over one approximately 12-hour period. The survey of Tuckernuck and Handkerchief Shoal was conducted slightly differently to obtain data five times over the tidal cycle over the relatively large survey area. Instead of collecting data continuously along the track lines at a low speed, data were collected for approximately 10 minutes at each discrete point (1-5 on each Shoal), with the boat steaming quickly between survey points.

Table 2-2. Station names, locations and dates for which current data were obtained (Figure 2-8)

Station	Location	Dates	Reference
Wd 20	41°33.9’ N, 70°03.8’ W	August 10-11, September 01- 02, 1852	F.J Haight, 1938 / M. Woodhill, 1850-53
Wd 22	41°31.8’ N, 70°01.2’ W	August 28-29, 1852	F.J Haight, 1938 / M. Woodhill, 1850-53
Wd 23	41°30.6’ N, 70°10.2’ W	August 9-10, 1852	F.J Haight, 1938 / M. Woodhill, 1850-53
Wd 29	41°29.6’ N, 70°03.5’ W	July 25-26, 1853	F.J Haight, 1938 / M. Woodhill, 1850-53
M-L	41°32.0’ N, 70°05.4’ W	August 12-13, 1857	F.J Haight, 1938 / H. Mitchel, 1857
M2	41°27.2’ N, 70°17.4’ W	July 8-9, 1857	F.J Haight, 1938 / H. Mitchel, 1857
M4	41°32.4’ N, 70°15.1’ W	July 13-14, 1857	F.J Haight, 1938 / H. Mitchel, 1857
L2 (Hedge Fence Lightship)	41°28.3’ N, 70°29.0’ W	September – December, 1913	F.J Haight, 1938
L3 (cross Rip Lightship)	41°26.9’ N, 70°17.5’ W	September – December, 1913	F.J Haight, 1938
L4 (Handkerchief Lightship)	41°29.3’ N, 70°04.0’ W	June – September, 1911 August, 1934 – August, 1935	F.J Haight, 1938
H21	41°32.0’ N, 70°25.7’ W	September 10-13, 1934	F.J Haight, 1938 / E.F. Hicks, 1934
H24	41°29.9’ N, 70°22.6’ W	July 30-August 2, 1934	F.J Haight, 1938 / E.F. Hicks, 1934

Table 2-2. Station names, locations and dates for which current data were obtained (continued)

Station	Location	Dates	Reference
H25	41°27.5’ N, 70°23.8’ W	August 8-17, 1934	F.J Haight, 1938 / E.F. Hicks, 1934
Monomy Point	41°33.0’ N, 70°01.3’ W	Current Predictions for June 3, 2002	Chart navigator, Maptech Inc., 2002
Monomy Point	41°33.5’ N, 70°09.0’ W	Current Predictions for June 3, 2002	Chart navigator, Maptech Inc., 2002
Handkerchief Lighted Whistle Buoy “H”	41°29.3’ N, 70°04.0’ W	Current Predictions for June 3, 2002	Chart navigator, Maptech Inc., 2002
Halfmoon Shoal	41°28.1’ N, 70°09.2’ W	Current Predictions for June 3, 2002	Chart navigator, Maptech Inc., 2002
Halfmoon Shoal	41°29.05’N, 70°11.55’W	Current Predictions for June 3, 2002	Chart navigator, Maptech Inc., 2002
Tuckernuck Shoal	41°24.3’ N, 70°10.4’ W	Current Predictions for June 3, 2002	Chart navigator, Maptech Inc., 2002
Muskeget	41°21.0’ N, 70°17.1’ W	Current Predictions for April 30, June 3, 2002	Chart navigator, Maptech Inc., 2002
Broken Ground – Horseshoe Shoal	41°33.0’ N, 70°17.1’ W	Current Predictions for April 30, 2002	Chart navigator, Maptech Inc., 2002
Cross Rip Channel	41°26.9’ N, 70°17.5’ W	Current Predictions for April 30, June 3, 2002	Chart navigator, Maptech Inc., 2002
Cape Poge Lt.	41°27.5’ N, 70°24.0’ W	Current Predictions for April 30, June 3, 2002	Chart navigator, Maptech Inc., 2002
Wreck Shoal - Eldridge Shoal	41°32.0’ N, 70°25.7” W	Current Predictions for April 30, 2002	Chart navigator, Maptech Inc., 2002

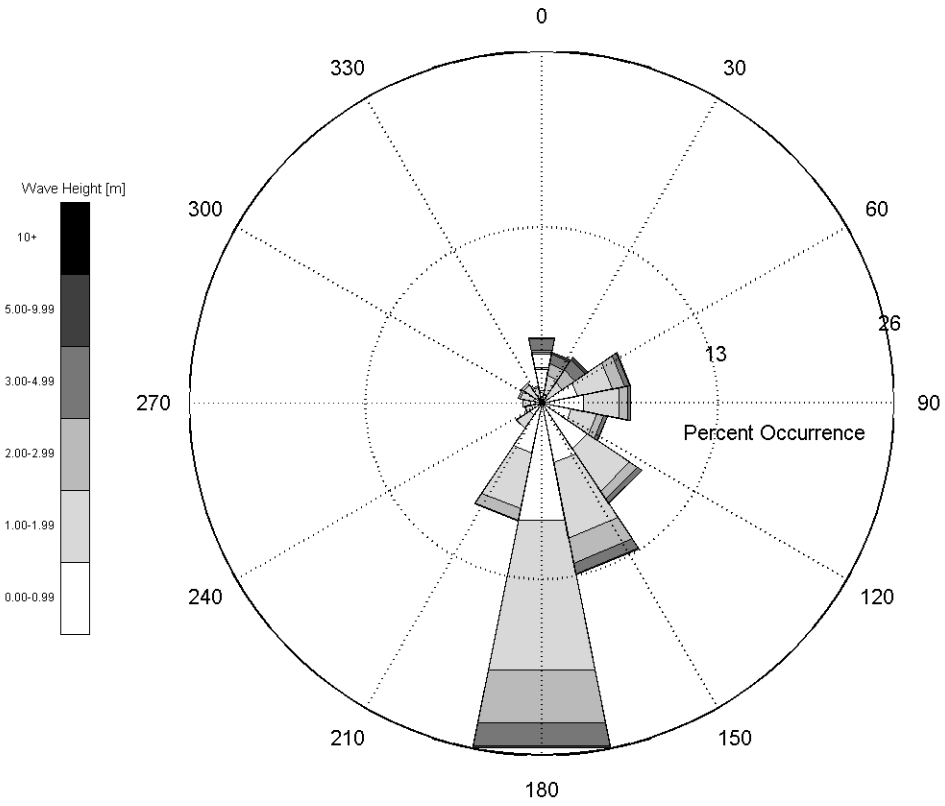

Figure 2-7. Wave rose for WIS Station 90 (1975-1995)

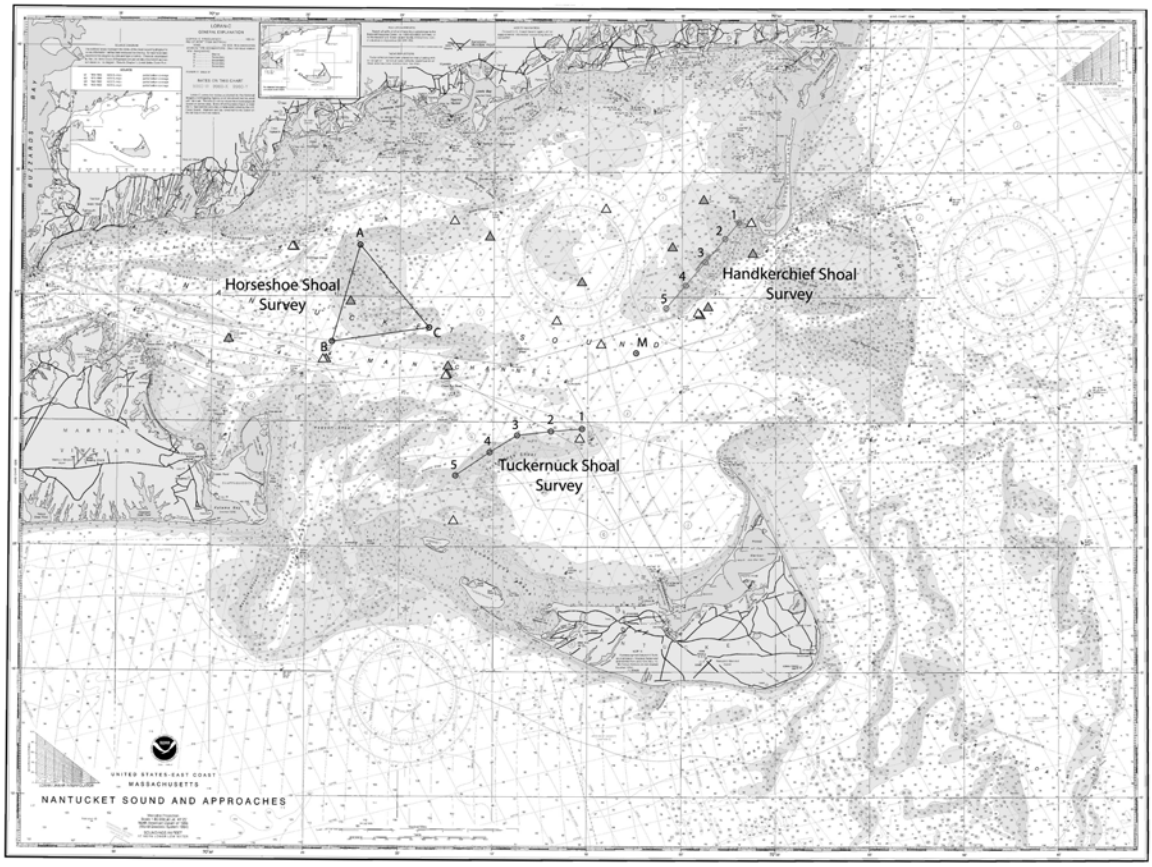

Figure 2-8. ADCP current survey tracklines and locations of existing current data (yellow triangles represent Maptech, Inc. (2002) data from Table 2-2 and orange triangles represent other previous data identified on Table 2-2)

3.0 Analytical Modeling

3.0 ANALYTICAL MODELING

Analytical models were applied to characterize existing wave, current, and sediment transport conditions at each of the three alternative wind farm sites. The models relied primarily upon the data described in Section 2.0, as well as analytical modeling tools and techniques. An overview of the technical approach for the analytical modeling is illustrated by Figure 3-1. First, a planning step was completed to refine the scope of work to meet project needs. Then, existing and new data sources were compiled to provide input directly to the wave, current, and sediment transport models. The wave and current model results then were evaluated to select appropriate conditions for the sediment transport modeling. The sediment transport model simulation results were finally combined with the data sets and the results from the wave and current models to develop conclusions pertinent to the wind farm project.

3.1 Wave Modeling

As described in Section 2.1, there are no direct wave measurements at the alternative sites, so the local wave climate was characterized using available wind data and an analytical model for wind wave generation within Nantucket Sound. Additionally, offshore wave data and information from the Atlantic Ocean were investigated as described in Section 2.1.4. Models were applied to simulate significant wave height and peak period based on historical wind measurements. Wave conditions were estimated for average wind conditions and the conditions defined as the average of the highest 10% wind speed, both segregated in to 22.5 degree wind directional bands. Details on the calculation methods and results are provided in this section

Winds blowing across Nantucket Sound (in any direction) generate waves that will impact the areas of interest around the shoals under investigation. Due to the sheltering of the Sound by the Islands and shoals, the major factors affecting the magnitude and period of the waves are: the fetch length (the distance over which wind acts on the water surface), average water depth, and wind speed. Local, historic wind data (collected at Nantucket Airport from 1986 to 2001) were used as the basis for the wind generated wave modeling as discussed in Section 2.

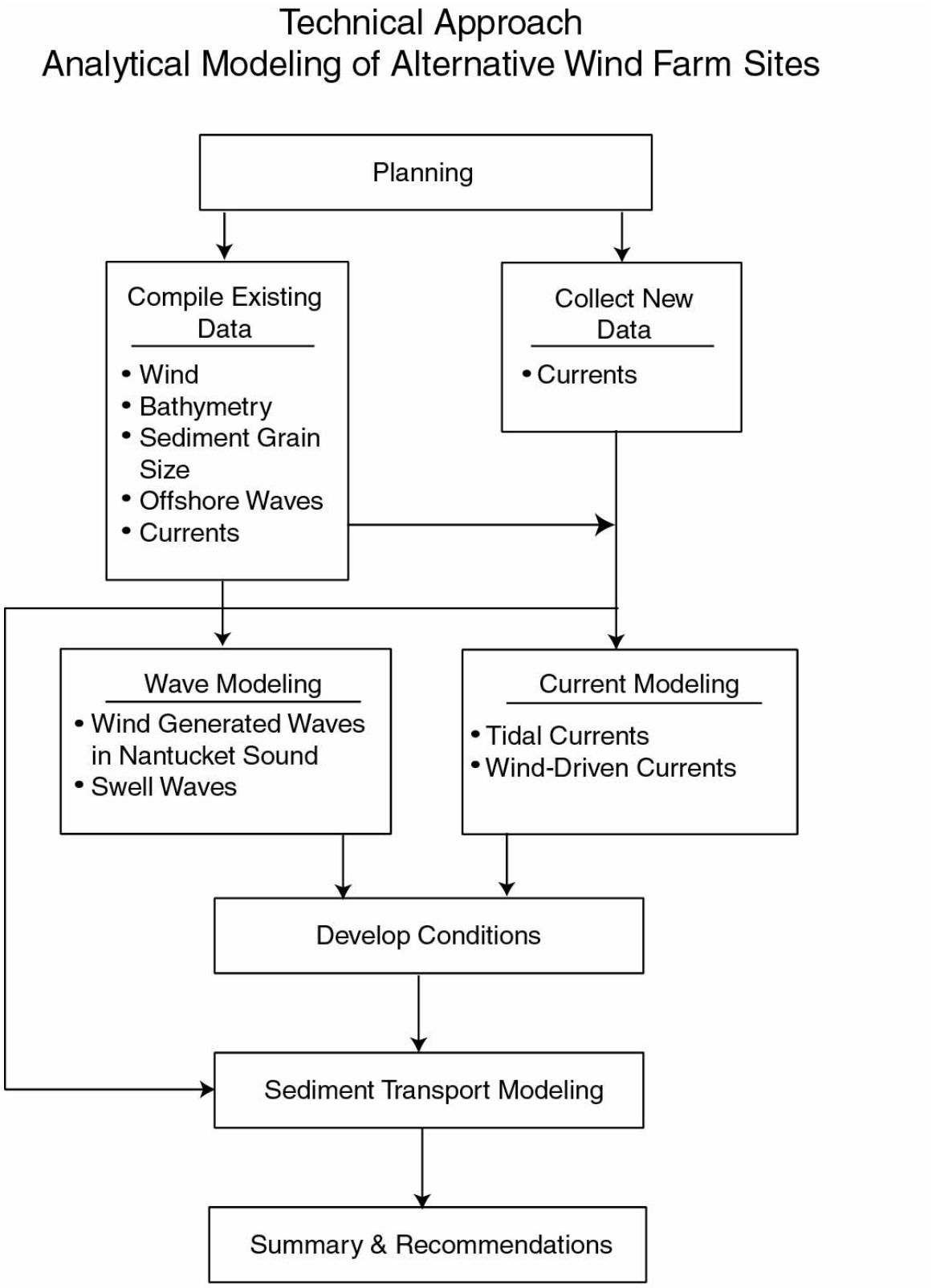

Figure 3-1. Technical approach for analytical modeling

Wind-generated waves were approximated using a computer model developed by the USACE. This computer model is part of the Automated Coastal Engineering System (ACES), published by the Coastal Engineering Research Center (USACE, 1992). The program is entitled *Wind Speed Adjustment and Wave Growth*, and provides simplified estimates for wave growth over open-water and restricted fetches, such as Nantucket Sound, in deep and shallow water. Although wind wave generation and growth incorporates complex physical processes that are not fully understood, simplified wave growth models provide useful estimates of wave heights and periods. Wind data, combined with estimates of fetch and depth from charts, were used to calculate estimates of wave height under selected conditions. The ACES model addresses only wind-generated waves, and does not account for the effects of refraction, diffraction, and non-linear effects. These effects would have to be characterized using a more detailed numerical model, likely a spectral refraction and diffraction model such as Simulating Waves Nearshore (SWAN) or Spectral Refraction Diffraction Model (REF/DIF-S). Detailed information regarding the theory of the analytical computer model used in this investigation can be found in the ACES user's manual (USACE, 1992) and the USACE Shore Protection Manual (1984).

Two key input parameters to the ACES program are the basin geometry and the average water depth of the fetch. Fundamentally, larger waves are generated as wind speed, water depth, and fetch length increase. Fetch is restricted within Nantucket Sound by Cape Cod, Monomoy Island, Nantucket Island, Marthas Vineyard, and surrounding shallow shoals. In order to characterize waves at Horseshoe, Tuckernuck, and Handkerchief Shoals, wave conditions were modeled corresponding to the range of wind direction and speed measured at Nantucket Airport. Wind statistics were determined, corresponding to the shoal-specific 22.5º directional bands shown in Figures 3-2 through 3-4. Direction bands that extend into the Atlantic Ocean were truncated at the limits of Nantucket Sound, because this modeling is intended only to characterize local sea conditions generated by wind within the Sound. Ocean swell conditions were not modeled. Instead, swell conditions were characterized based on offshore wave information as described at the end of this section. In combination, these directional bands encompass the full range of wind conditions that can produce different wave conditions in terms of wave height and period. Table 3-1 summarizes the mean wind speed, average of the highest 10 percent of wind speeds, fetch length, and average water depth for each directional bin at each site. Wind statistics were computed from hourly measurements, sorted into 22.5 degree directional bands. These wind conditions provided the input for the wave modeling. Significant wave height and peak period were computed for each combination of wind speed and direction.

A total of 96 wave model (ACES) simulations were performed. ACES model output are summarized in Table 3-2, including significant wave height (H_s), peak period (T_p), and peak direction. Significant wave height is statistically defined as the average height of the highest one-third waves in a sea state, and is a typical statistic used for coastal engineering applications. Studies have shown that reported visual shipboard observations of wave height are approximately equal to the significant wave height. The spectral peak period is the wave period that characterizes the majority of the waves in a sea state (i.e., the frequency at which the most energy resides).

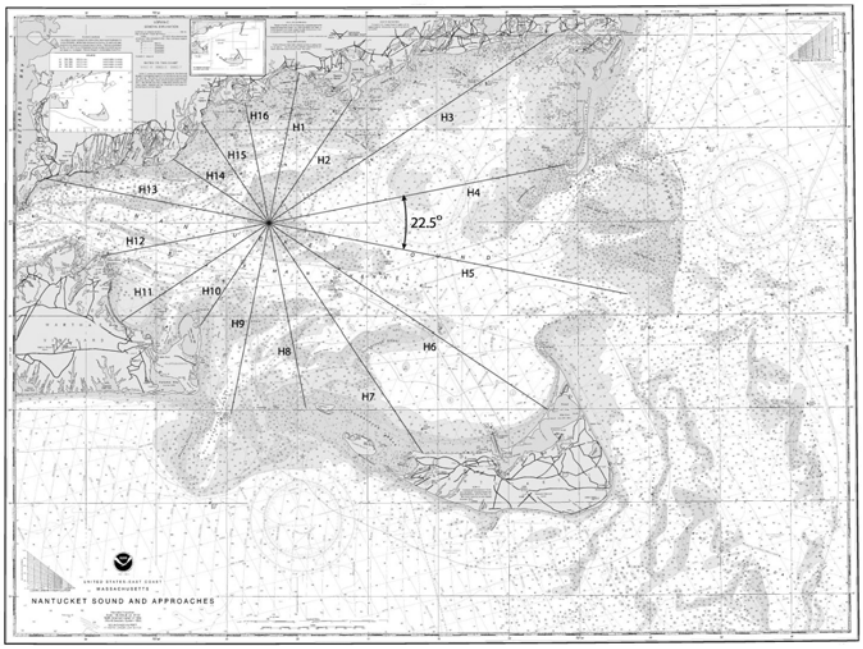

Figure 3-2. Fetch directions for Horseshoe Shoal

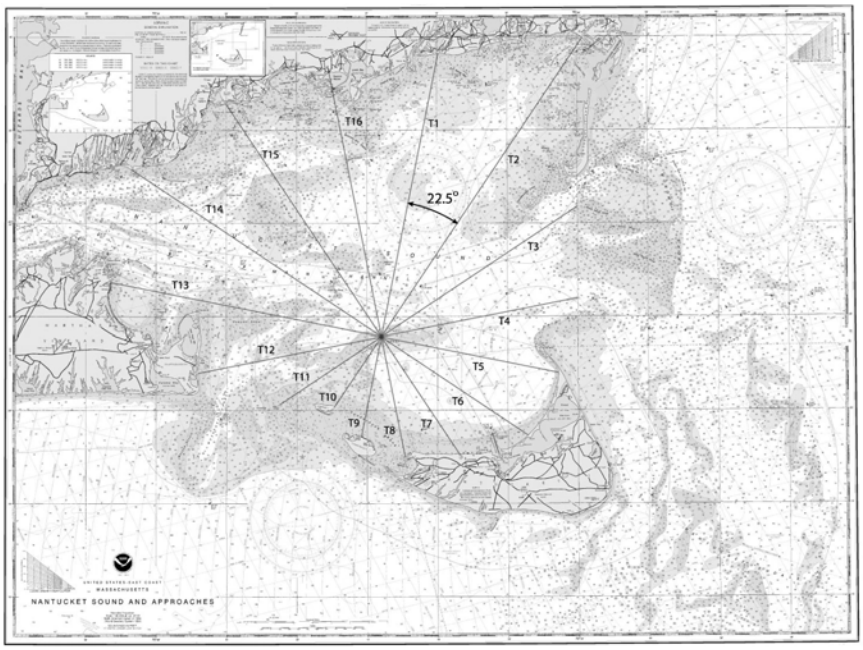

Figure 3-3. Fetch directions for Tuckernuck Shoal

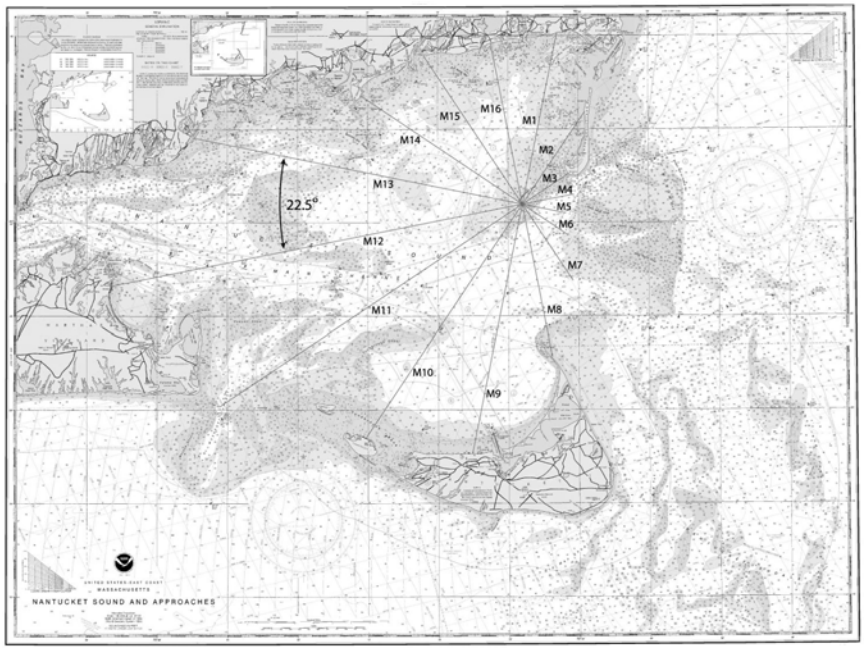

Figure 3-4. Fetch directions for Handkerchief Shoal

The wave modeling results in Table 3-2 represent wave conditions at the center of each alternative site. Generally, Horseshoe Shoal are exposed to the largest waves from the easterly directions, Handkerchief Shoal are exposed to the largest waves from the south and west directions, and Tuckernuck Shoal are exposed to the largest waves from the northerly directions. This is the expected result based on the visual representation of fetch length exposure shown in Figures 3-2 through 3-4, in that the highest waves are derived from the longest fetches. Locally-generated significant wave heights are typically in the range of 1 to 4 feet, although individual wave heights can be higher. Substantially higher waves will be present during storms. Spectral peak periods for the locally generated wind waves are relatively short, between 2 and 4 seconds. The wave data that will be collected at the met-ocean tower will provide valuable data for ground-truthing wave modeling results at the Horseshoe Shoal site.

With this characterization of wave conditions at each site, the next step was to characterize the spatial variation of wave height within each alternative site. In order to obtain a distribution of wave heights over the shoals, a shoaling coefficient and wave breaking criteria were applied to the wind-generated waves at the center of each location (USACE, 1984).

Table 3-1. Relative wind speeds and directions for the locations of interest

	HORSESHOE SHOAL ORIGIN AT 41 30N 70 22W					
Fetch NO	**Directional Bin from**	**to**	**Mean Wind Speed (mph)**	**Avg. of Highest 10% Wind Speed (mph)**	**Fetch Length mi**	**Average Depth ft**
H1	0	22.5	14.8	28	8.6	20
H2	22.5	45	15.2	29	9	22
H3	45	67.5	13.7	25	20.4	23
H4	67.5	90	11.9	24	18.2	28
H5	90	112.5	12.6	25	17.7	38
H6	112.5	135	13.4	26	20.4	29
H7	135	157.5	12.5	24	16.5	21
H8	157.5	180	11.8	23	11.2	20
H9	180	202.5	11.3	21	12.2	32
H10	202.5	225	11.8	22	6.9	27
H11	225	247.5	13.0	23	10.8	26
H12	247.5	270	14.1	24	10.2	34
H13	270	292.5	13.6	25	13	19
H14	292.5	315	14.3	25	6.9	12
H15	315	337.5	14.6	25	7.1	14
H16	337.5	360	14.3	26	7.2	18
	TUCKERNUCK SHOAL ORIGIN AT 41 24N 70 14W					
Fetch NO	**Directional Bin from**	**to**	**Mean Wind Speed (mph)**	**Avg.High.10% Wind Speed (mph)**	**Fetch Length mi**	**Average Depth ft**
T1	0	22.5	14.8	28	17.5	30
T2	22.5	45	15.2	29	21.7	24
T3	45	67.5	13.7	25	14.8	33
T4	67.5	90	11.9	24	13.8	27
T5	90	112.5	12.6	25	10.9	29
T6	112.5	135	13.4	26	10.4	30
T7	135	157.5	12.5	24	8.3	22
T8	157.5	180	11.8	23	7	26
T9	180	202.5	11.3	21	6.4	17
T10	202.5	225	11.8	22	5	14
T11	225	247.5	13.0	23	6.2	19
T12	247.5	270	14.1	24	11.2	19
T13	270	292.5	13.6	25	16.7	21
T14	292.5	315	14.3	25	18	36
T15	315	337.5	14.6	25	16.9	22
T16	337.5	360	14.3	26	15.5	26
	HANDKERCHIEF SHOAL ORIGIN AT 41 31N 70 04W					
Fetch NO	**Directional Bin from**	**to**	**Mean Wind Speed (mph)**	**Avg.High.10% Wind Speed (mph)**	**Fetch Length mi**	**Average Depth ft**
M1	0	22.5	14.8	28	10.3	18
M2	22.5	45	15.2	29	5.2	11
M3	45	67.5	13.7	25	3	8
M4	67.5	90	11.9	24	3.8	20
M5	90	112.5	12.6	25	3.5	21
M6	112.5	135	13.4	26	3.4	22
M7	135	157.5	12.5	24	4.4	25
M8	157.5	180	11.8	23	8.4	26
M9	180	202.5	11.3	21	15.6	30
M10	202.5	225	11.8	22	17.2	22
M11	225	247.5	13.0	23	21.5	27
M12	247.5	270	14.1	24	25.6	30
M13	270	292.5	13.6	25	20.5	26
M14	292.5	315	14.3	25	11.9	20
M15	315	337.5	14.6	25	10.6	21
M16	337.5	360	14.3	26	9.7	22

A subset of the wave conditions presented in Table 3-2 was selected for more detailed spatial modeling. Three scenarios were selected for each site as the basis for the sediment transport modeling in Section 3.3: Scenario (1) largest waves approaching from a direction corresponding to the flood and ebb current directions; Scenario (2) waves approaching from the most frequent wind direction; and Scenario (3) waves approaching from any direction with the largest amplitude.

Wave height was calculated from the shoaling coefficient as a function of water depth throughout each site based on the bathymetry presented in Section 2. A depth-limited wave breaking criteria was applied to limit the maximum wave height to 78 percent of the local water depth. For simplicity, refraction and diffraction processes were left out.

Figures 3-5, 3-6, and 3-7 illustrate representative significant wave height distributions for each alternative site. The color bar indicates the magnitude of the wave height, and the underlying solid black lines represent the bathymetric contours. Figures 3-5(a), 3-6(a), and 3-7(a) illustrate wave height distributions for local wind wave conditions H6, T2, and M12, corresponding to Table 3-2, for Horseshoe Shoal, Tuckernuck Shoal, and Handkerchief Shoal, respectively. These examples were selected for illustration, because they correspond to the largest significant wave height for the locally-generated wave conditions modeled using ACES (Scenario 3 for each site). The figures show that wave height is modified in the shallow portions of the shoals due to wave shoaling and breaking, for the locally-generated wind waves in Nantucket Sound.

While ACES was used to characterize waves generated by winds within Nantucket Sound, it also is possible that longer period waves enter Nantucket Sound from the Atlantic Ocean. A previous study (Goud and Aubrey, 1985) closer to shore, which studied waves offshore Popponesset Island for a one-month period, did not indicate the existence of a significant offshore swell component. However, these data do not provide conclusive results regarding the absence of swell in the Sound, particularly at the offshore shoals identified as alternative wind farm sites. As such, a conservative estimate of long period swell conditions was developed for this investigation. Results are shown in Figures 3-5(b), 3-6(b), and 3-7(b). These figures represent average offshore waves approaching from easterly through southeasterly directions provided by WIS Station 2090 (41.50N 69.75W), east from Monomoy Island within the Atlantic Ocean. The average incident wave height for these directions is 4.5 ft, and the wave period is 8 seconds. Average ocean waves were selected for analysis to capture the potential effects for longer period waves on the sites, since more active sediment transport was anticipated for ocean swell as compared to the short-period, locally-generated wind waves in the Sound. Although significantly higher and longer period waves occur in the Ocean (e.g., heights greater than 20 feet with periods exceeding 12 seconds), it was not judged appropriate to assume such large waves occurred in the Sound. The modeling approach is already appropriately conservative, since waves propagating from offshore to onshore are likely modified substantially by the complex and shallow shoal structure separating Nantucket Sound from the Ocean, as well as by the relatively narrow

Table 3-2. Wave heights and periods resulting from the ACES model

HORSESHOE SHOAL			Avg. Winds			Avg.of Highest 10% Wind		
Fetch NO	Directional Bin from	To	Hs ft	Tp sec	MWD Deg	Hs ft	Tp sec	MWD deg
H1	0	22.5	1.4	2.3	51	2.5	3.2	51
H2	22.5	45	1.8	2.7	56	3.2	3.6	56
H3	45	67.5	1.7	2.6	60	3.1	3.5	60
H4	67.5	90	1.5	2.4	68	3.0	3.4	68
H5	90	112.5	1.6	2.5	114	3.3	3.6	114
H6	112.5	135	1.8	2.6	123	3.4	3.6	123
H7	135	157.5	1.5	2.4	130	2.8	3.3	130
H8	157.5	180	1.3	2.2	145	2.4	3.1	145
H9	180	202.5	1.2	2.2	187	2.3	3.0	187
H10	202.5	225	1.1	2.1	193	2.2	2.9	193
H11	225	247.5	1.3	2.3	240	2.3	3.0	240
H12	247.5	270	1.5	2.4	275	2.6	3.1	275
H13	270	292.5	1.4	2.4	279	2.5	3.1	279
H14	292.5	315	1.3	2.3	283	2.1	2.9	283
H15	315	337.5	1.1	2.1	288	1.9	2.7	288
H16	337.5	360	1.1	2.0	4	1.9	2.7	4
TUCKERNUCK SHOAL			**Avg. Winds**			**Avg.of Highest 10% Wind**		
Fetch NO	Directional Bin from	to	Hs ft	Tp sec	MWD Deg	Hs ft	Tp sec	MWD deg
T1	0	22.5	1.9	2.7	27	3.6	3.7	27
T2	22.5	45	2.0	2.8	32	3.6	3.8	32
T3	45	67.5	1.8	2.6	38	3.2	3.5	38
T4	67.5	90	1.3	2.3	72	2.7	3.2	72
T5	90	112.5	1.3	2.3	84	2.7	3.2	84
T6	112.5	135	1.4	2.3	118	2.7	3.2	118
T7	135	157.5	1.0	2.0	129	2.0	2.7	129
T8	157.5	180	0.9	1.9	154	1.8	2.6	154
T9	180	202.5	0.8	1.8	183	1.5	2.4	183
T10	202.5	225	0.7	1.7	253	1.4	2.3	253
T11	225	247.5	1.0	2.0	269	2.1	2.8	269
T12	247.5	270	1.4	2.3	280	2.5	3.1	280
T13	270	292.5	1.7	2.6	288	2.9	3.4	288
T14	292.5	315	1.9	2.7	304	3.3	3.5	304
T15	315	337.5	1.8	2.6	320	2.9	3.4	320
T16	337.5	360	1.7	2.6	360	3.1	3.4	360
HANDKERCHIEF SHOAL			**Avg. Winds**			**Avg.of Highest 10% Wind**		
Fetch NO	Directional Bin from	to	Hs ft	Tp sec	MWD Deg	Hs ft	Tp sec	MWD deg
M1	0	22.5	1.4	2.3	7	2.6	3.1	7
M2	22.5	45	1.1	2.1	12	1.9	2.8	12
M3	45	67.5	0.8	1.8	17	1.3	2.3	17
M4	67.5	90	0.7	1.6	81	1.3	2.2	81
M5	90	112.5	0.7	1.6	93	1.4	2.2	93
M6	112.5	135	0.8	1.7	171	1.5	2.4	171
M7	135	157.5	1.1	2.1	185	2.1	2.9	185
M8	157.5	180	1.3	2.2	192	2.7	3.2	192
M9	180	202.5	1.3	2.3	200	2.5	3.1	200
M10	202.5	225	1.4	2.4	232	2.6	3.2	232
M11	225	247.5	1.8	2.6	251	3.1	3.5	251
M12	247.5	270	2.0	2.8	258	3.4	3.7	258
M13	270	292.5	1.8	2.6	265	3.3	3.6	265
M14	292.5	315	1.7	2.6	278	2.8	3.3	278
M15	315	337.5	1.4	2.4	288	2.4	3.1	288
M16	337.5	360	1.4	2.3	341	2.5	3.1	341

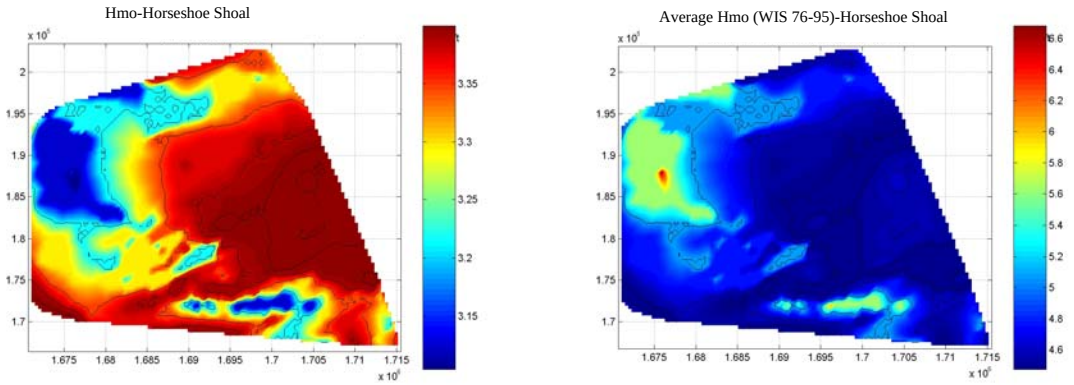

a) Local wind waves (H6) **b) Ocean swell**

Figure 3-5. Significant wave height distribution around Horseshoe Shoal

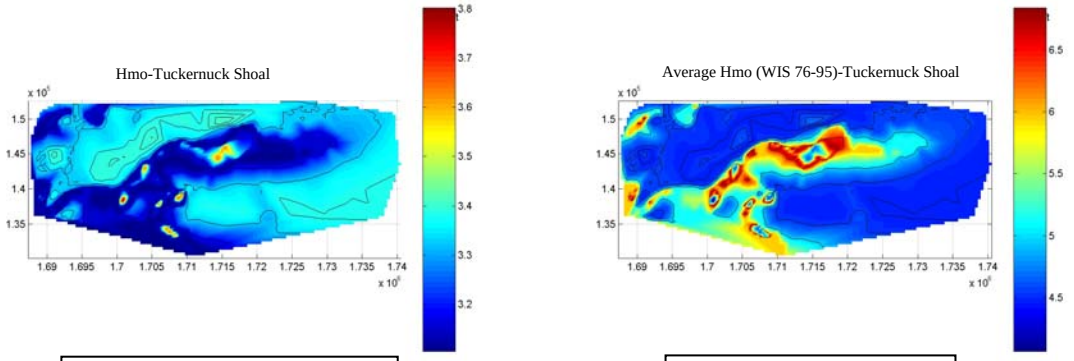

a) Local wind waves (T2) **b) Ocean swell**

Figure 3-6. Significant wave height distribution around Tuckernuck Shoal

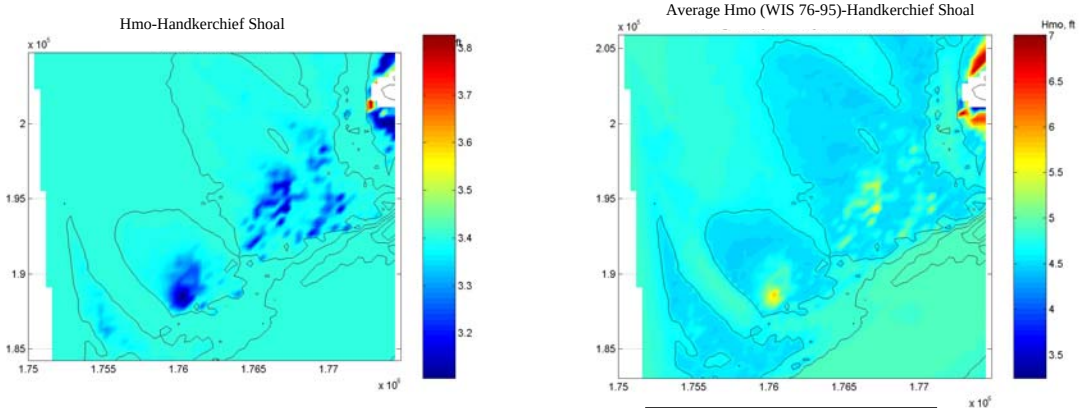

a) Local wind waves (M12) **b) Ocean swell**

Figure 3-7. Significant wave height distribution around Handkerchief Shoal

gaps between Monomoy Island and Nantucket Island to the east and between Nantucket Island and Martha's Vineyard to the south. Waves experience shallow water wave transformations such as shoaling, refraction, diffraction, reflection, and frictional energy dissipation. However, for this analysis, only a shoaling coefficient was used to modify the offshore swell waves. As such, the representation of longer period waves in Figures 3-5(b) through 3-7(b) is conservative.

These wave height distributions (both locally wind-generated waves and ocean swell) were used to generate wave-induced bottom velocities required for the sediment transport modeling in Section 3.3. This modeling also incorporated a range of tidal current conditions, as summarized by Table 3-3.

3.2 Current Modeling

3.2.1 Tidal Currents

Examination of the available current data presented in Section 2.1.5 reveals that during the flood, the flow in Nantucket Sound is generally to the east, and the flow reverses direction during the ebb. The intensity of tidal flow, in general, decreases from west to east. Some local variations of current speed and direction occur along and across the Sound due to shoreline configuration and local bathymetry (Redfield, 1980). However, the available data do not show clearly how flow characteristics can vary on small spatial scales, such as on scales of several miles in the vicinity of the alternative wind farm sites.

As such, a specific objective of this work was to investigate details of the flow for three specific locations, namely for the areas of the Horseshoe, Handkerchief, and Tuckernuck Shoals. The technical approach was to collect data on ocean currents at each specific area of interest (Section 2.2), compare these data with historical field observations of tidal currents in the Sound, and analyze spatial variations of the flow on small scales over the shoals. The aim was to ascertain a relationship between flow characteristics and bottom topography for each specific location. The maximum flood and ebb current velocities for each period of observations, including historical observations, were compared with/referenced to the magnitude of sea surface elevation at Oak Bluffs, Martha's Vineyard. In that manner, the final outcome of the comparison was a representative field of ebb and flood currents for each alternative site for the mean tide and spring tide conditions.

Figures 3-8 through 3-10 summarize the results of the current data analysis. Each of these polar plots contain vectors that indicate the speed and direction of tidal currents (ebb and flood) at discrete survey points within the three alternative sites. Information on Figures 3-8 through 3-10 was taken directly from the ADCP surveys discussed in Section 2.2. Figure 3-8 is for Horseshoe Shoal, and provides current information for points A, B, and C corresponding to the vertices of the triangular survey track. Currents at points A and B are directed slightly to the north and south, respectively, indicating that tidal flow is re-directed away from the shallowest portions of the shoal. Currents at point C are directed along the axis of the small channel or the southeast side of the shoal. Flood currents flow primarily to the east and are stronger than the westerly-directed ebb

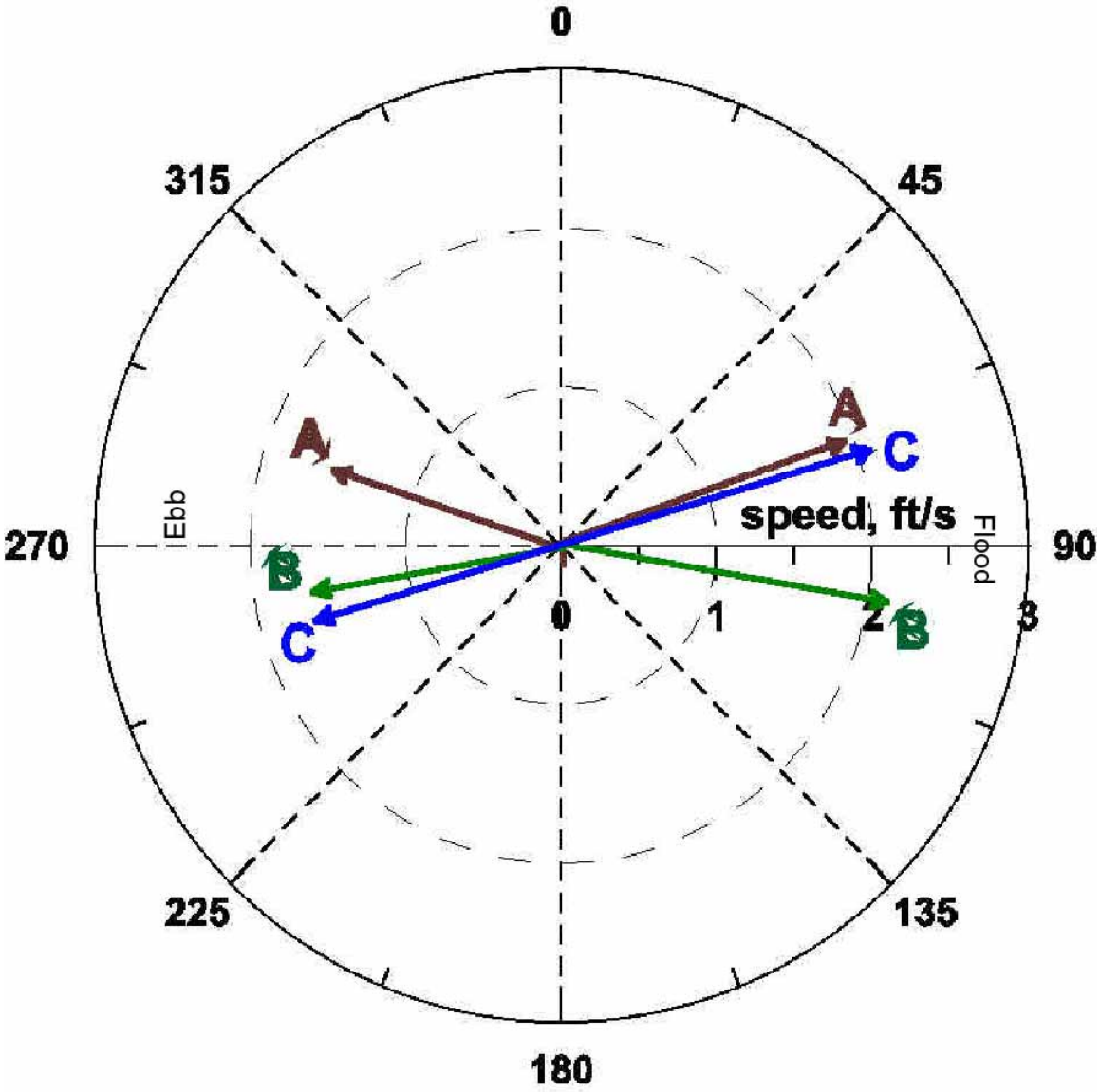

Figure 3-8. Vector representation of tidal currents in areas A, B, and C on Horseshoe Shoal (Figure 2.8).

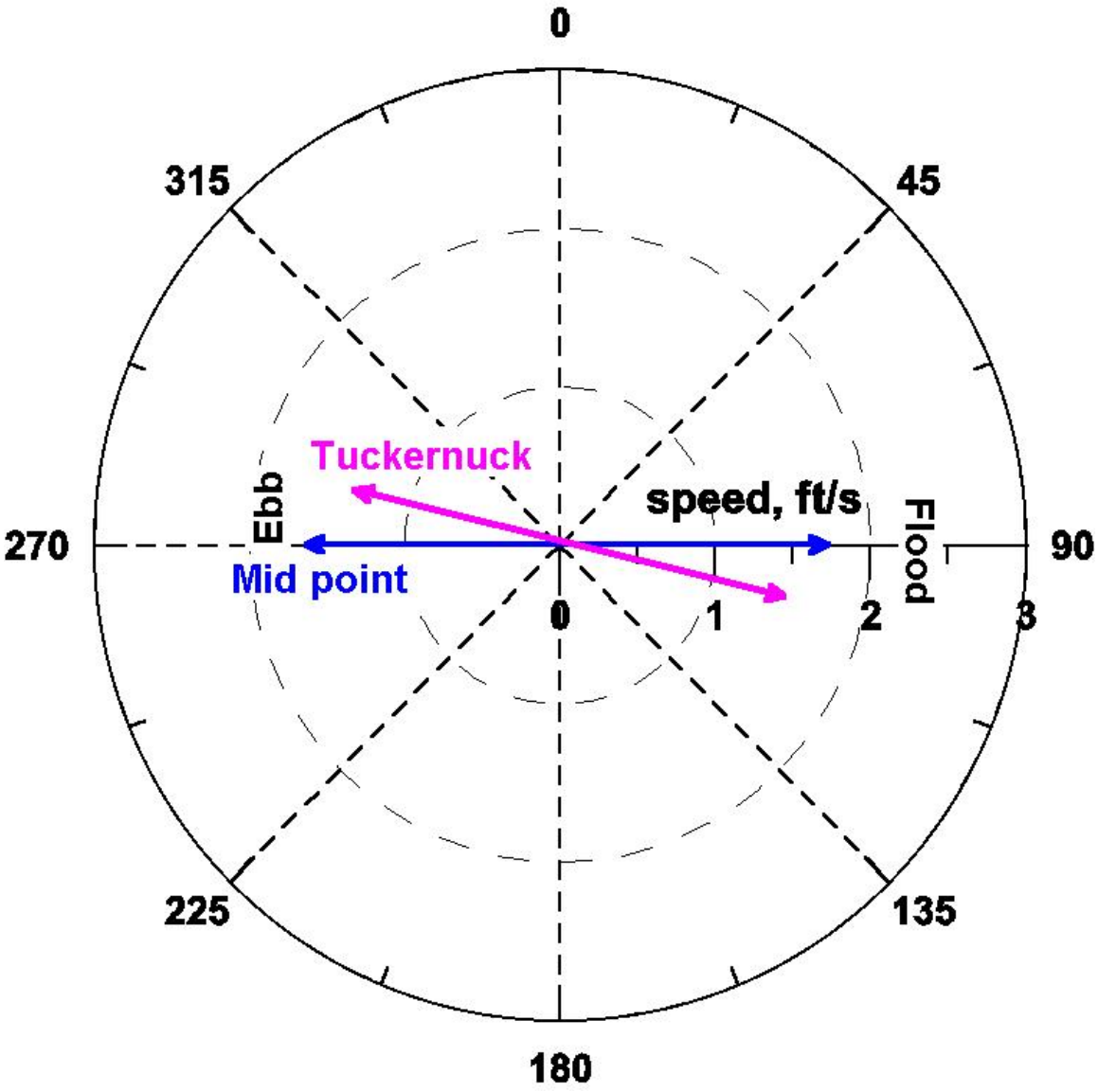

Figure 3-9. Vector representation of tidal currents at Tuckernuck Shoal

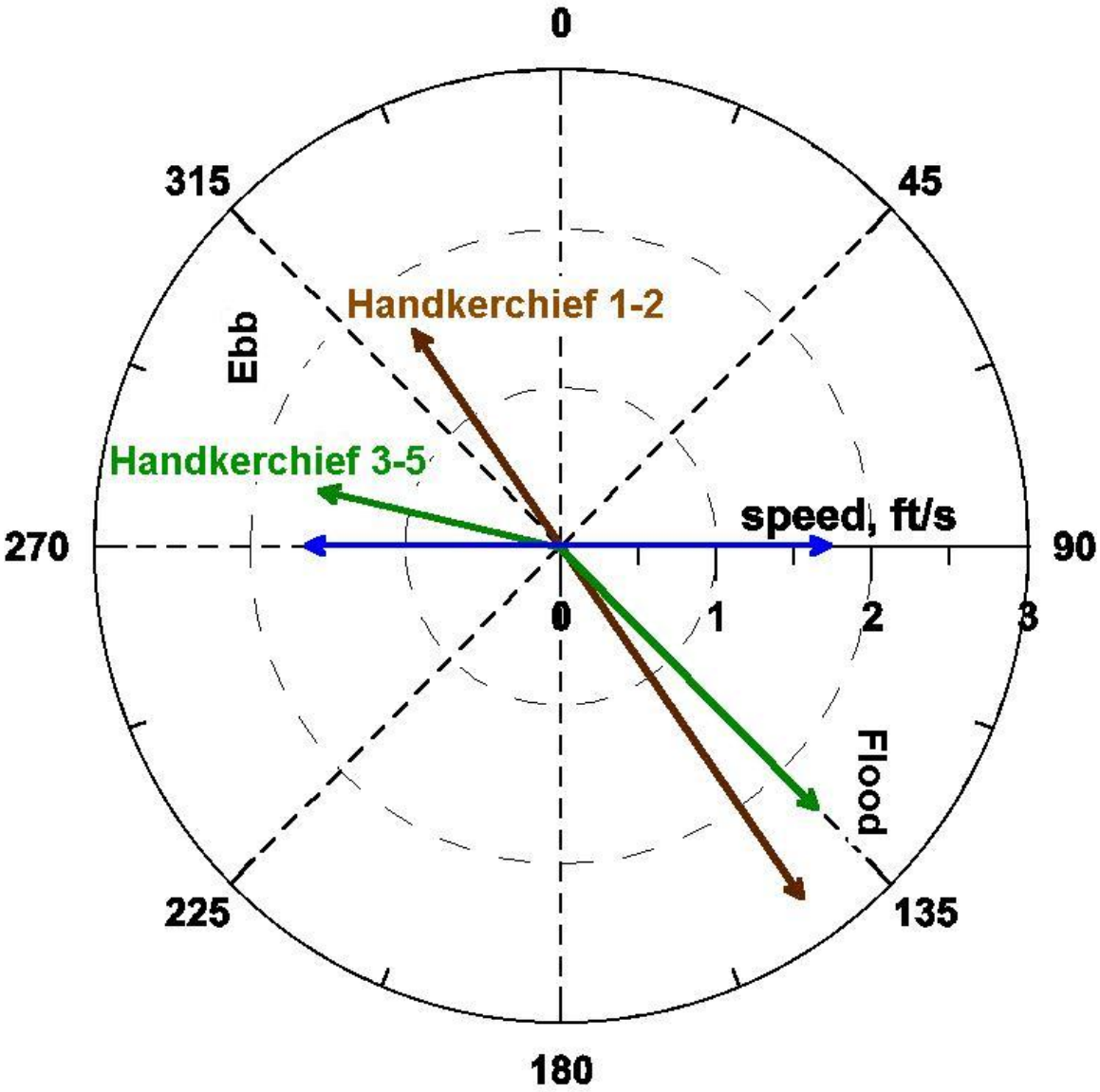

Figure 3-10. Vector representation of tidal currents at Handkerchief Shoal

currents. Figure 3-9 shows the currents at Tuckernuck Shoal, which have a west-northwest sense on the ebb, and a east-southeast sense on the flood. These directions differ slightly from currents in the center of the Sound (point M on Figure 2-7), which have an east/west sense. Flood currents at Tuckernuck Shoal are slightly stronger than ebb currents. Figure 3-10 illustrates flood and ebb current patterns at Handkerchief Shoal. Directions at survey points 1-2 differed from current directions at points 3-5, due to the proximity to Monomoy Island. Currents at points 1 and 2 are in the lee of the Island, and are directed more in line with the shoreline/shoal system. Currents on the flood tide at Handkerchief Shoal also are stronger that the ebb currents.

Overall, the survey and historical current data were consistent, and provided adequate information to characterize the spatial variation of flood and ebb currents at each site. The main conclusions based on the data were:

- Easterly-directed flood tide currents are generally stronger than westerly-directed ebb currents, which provide a mechanism for net easterly transport of water-borne substances or sediments.
- Current speed and direction varies more with space than with water depth in response to shoreline configuration, as well as shoal geometry.

Based on the survey and the historical data, gridded fields of tidal currents (corresponding to the same gridded regions used in the wave modeling) were developed for each alternative site. Four different tidal current regime scenarios were produced for each of the three gridded regions: flood mean, flood spring, ebb mean, and ebb spring. A linear interpolation approach between measurement locations was used to construct the grid for both flood and ebb conditions. A combination of the ADCP current data with historical measurements provided enough discrete data points to span the regions of interest, and data for the basis for interpretation. The interpolation procedure did not account for dynamic principles, continuity, or conservation of mass.

Figures 3-11, 3-12, and 3-13 illustrate the estimated current field at each of the alternative sites. The color bar corresponds to the magnitude of the tidal current, arrows show the direction and the relative magnitude, and the solid black line represents the underlying bathymetry for each of the alternative site.

Generally, flood currents in the Sound are directed toward the east, and ebb tide currents are directed toward the west. Spring tide currents tend to be 15-20 percent more swift than mean tide currents. At Horseshoe Shoal, the swiftest currents occur on the northwest portion of the shoal. At Tuckernuck Shoal, the swiftest currents occur along the western bank of the shoal. Flood tide currents at Tuckernuck shoal have more of a northerly component (directly east-northeast), and ebb tide currents have a east-southeast sense, which is consistent with historical data. Due to the location of Handkerchief Shoal on the west side of Monomoy Island, tidal currents are directed southeast and northwest on the flood and ebb tides, respectively. Tidal currents also are most swift at Handkerchief Shoal due to its shallow nature and proximity to the tidal constriction between Monomoy Island and Nantucket Island that separates the Ocean from Nantucket Sound. Tidal flow is concentrated and redirected in the vicinity of the Handkerchief Shoal as the Sound meets the Atlantic Ocean.

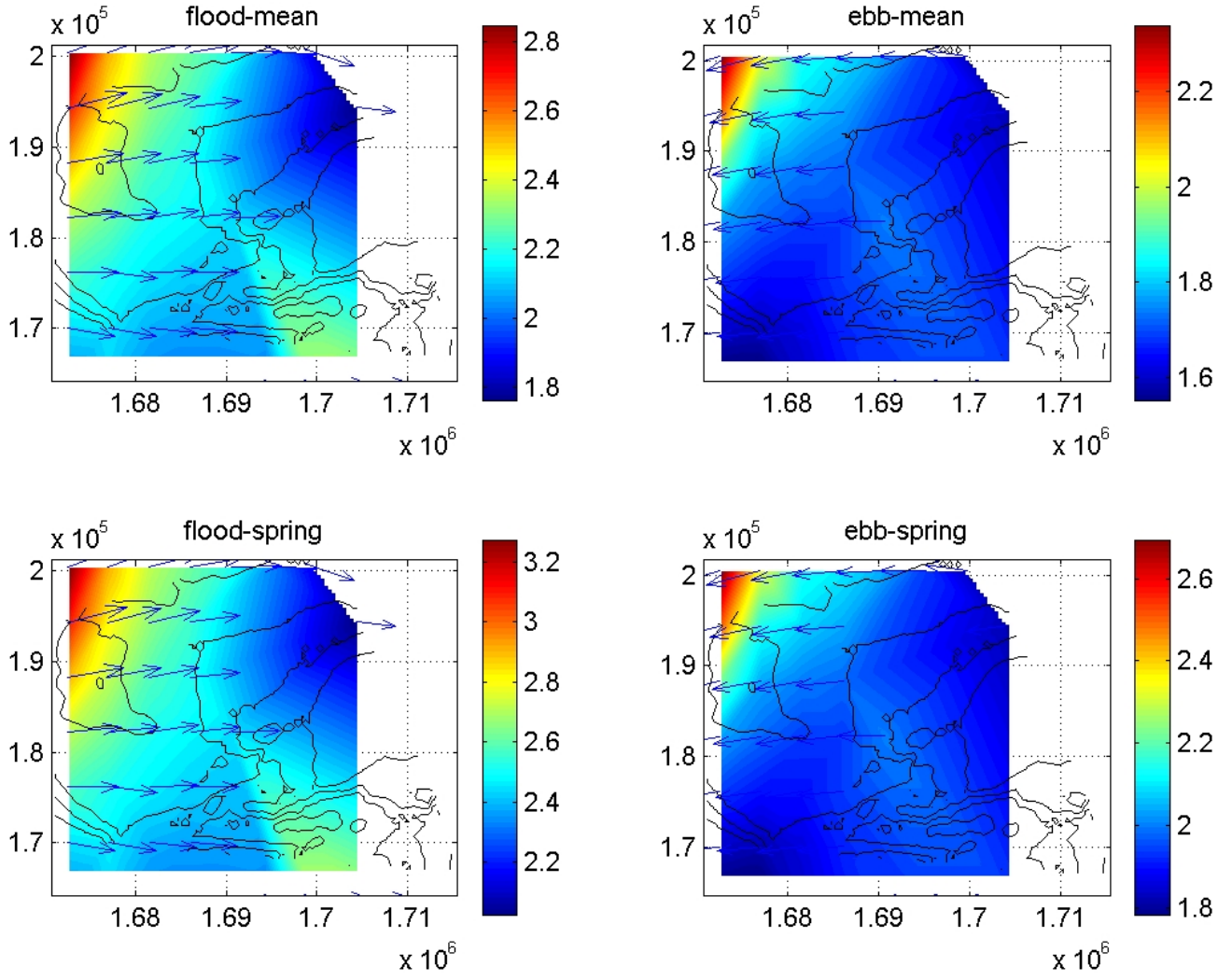

Figure 3-11. Estimated tidal currents (ft/s) at Horseshoe Shoal

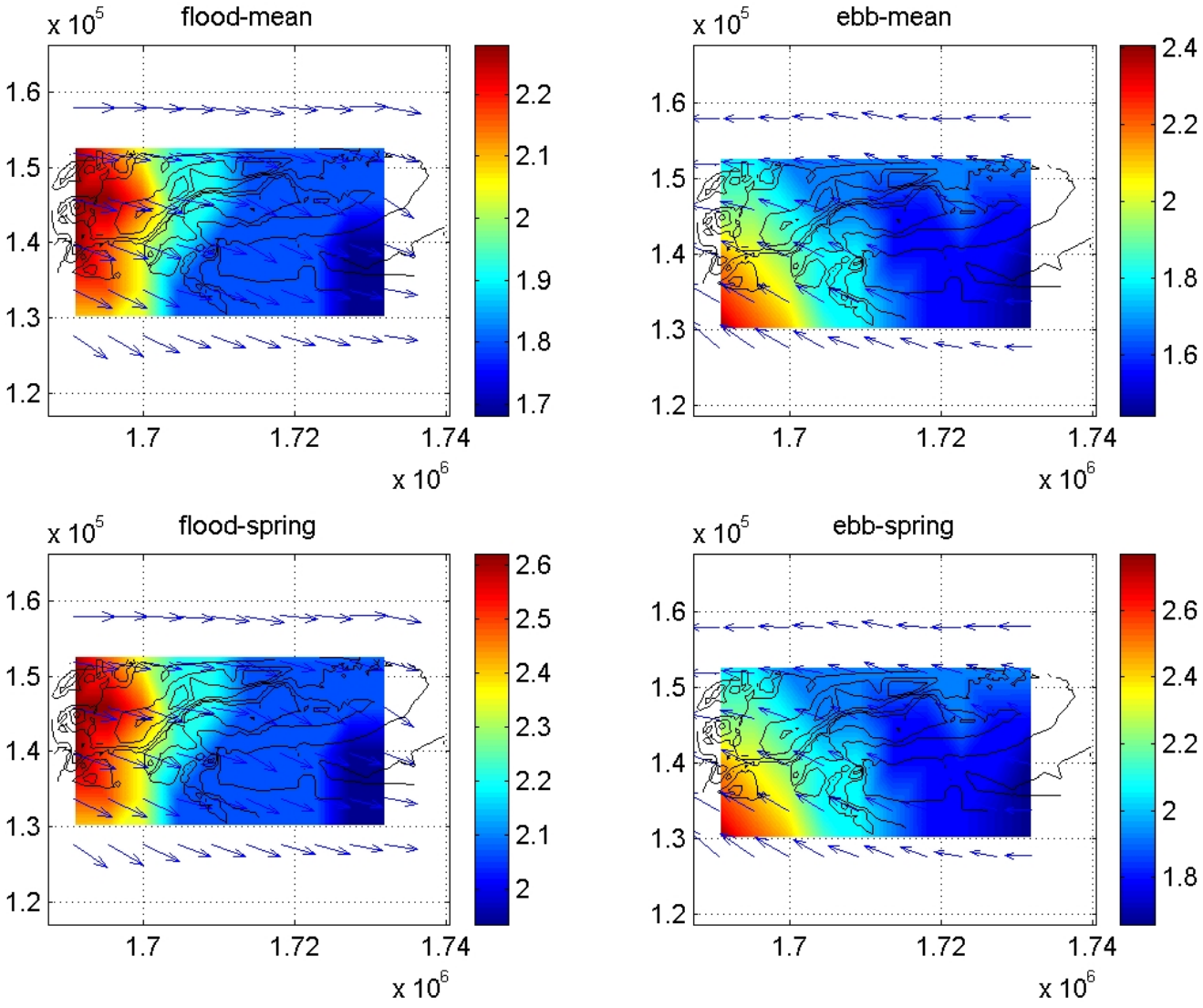

Figure 3-12. Estimated tidal currents (ft/s) at Tuckernuck Shoal

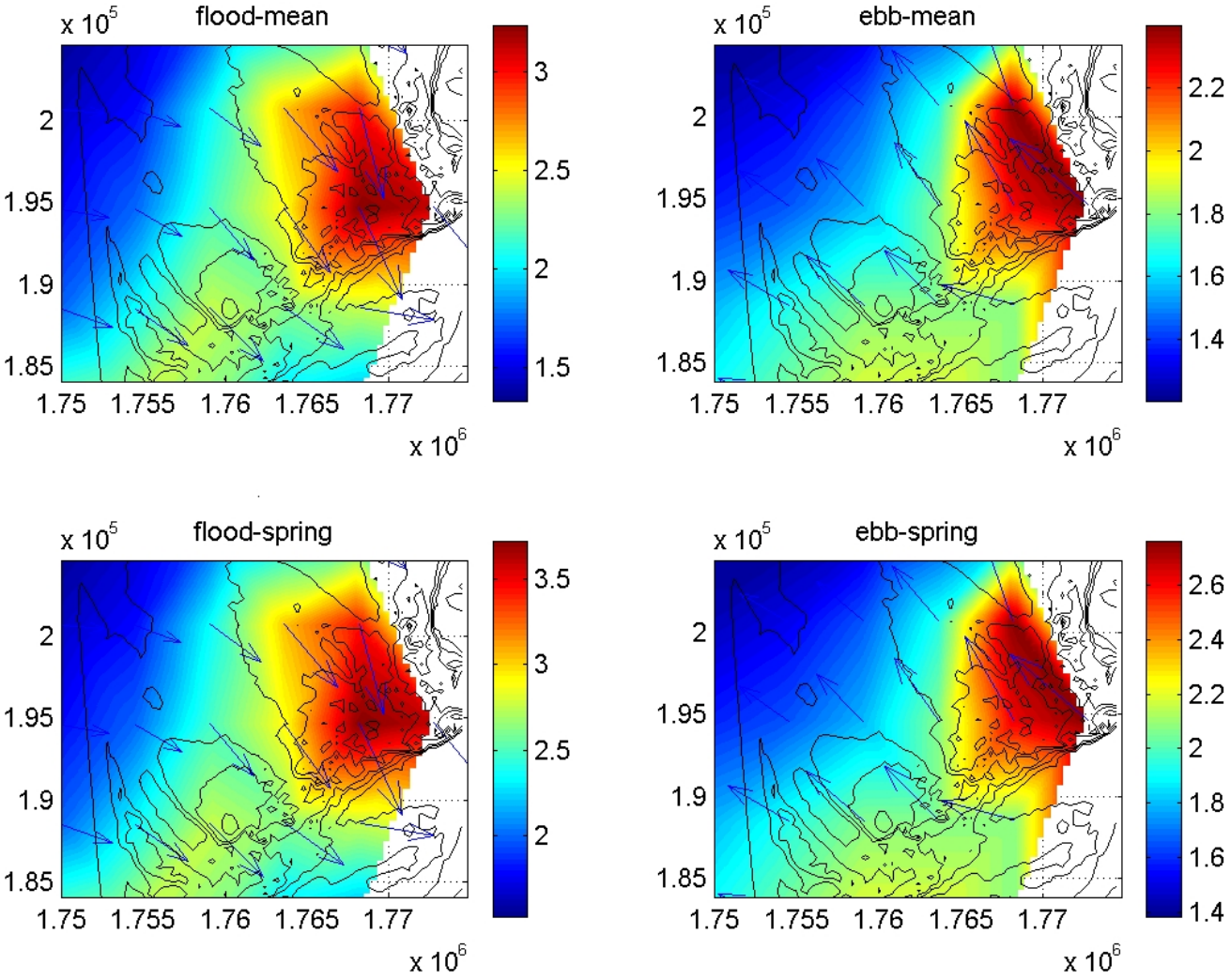

Figure 3-13. Estimated tidal currents (ft/s) at Handkerchief Shoal

3.2.2 Wind-Driven Currents

In addition to tidal currents, other currents can develop within Nantucket Sound as a result of winds and tidal forcing interacting nonlinearly with bathymetry. These residual currents are generally small compared to the tidal currents, but can induce a net flow in a direction other than the dominant ebb or flow direction, and can affect transport of water-borne substances and/or sediments. As such, an analytical model of residual currents was developed and applied to simulate tidal currents (extending the analysis presented in 3.2.1) and compare the relative speeds of residual and tidal currents.

The analytical model of wind-driven currents also was required because the wind-driven component of the currents could not be isolated from the current survey data. Meteorological conditions during the Horseshoe Shoal survey were characterized by

westerly winds with speeds greater than 10 knots. On June 3 the wind was from the northwest and the wind speed reached 20 knots. Although winds were appreciable, the wind-driven component of the current could not be isolated in the field data. This could serve to confirm the hypothesis that wind-driven currents are small compared to tidal currents, but could also suggest that conditions during the survey were not conducive to the development of measurable wind-driven currents (e.g., sustained high winds).

The model calculations of wind-driven and tidal currents were based on the depth-averaged, linearized, mass and momentum equations for a constant-density fluid, with a rigid lid and a linearized representation of bottom drag (e.g., Pedlosky, 1979). The theoretical development of the wind-driven current model is presented in Appendix B, and these equations are defensible as a first order approximation in the present application. The deviation resulting from the fundamental equations result in an elliptic equation for the transport stream function, which is solved by an iterative relaxation method (e.g., Press et al., 1989). The computational domain is a 151-by-151 grid of equally spaced nodes, with a constant ambient depth and an elongated, elliptical shoal representing Horseshoe Shoal. Boundary conditions of no flow normal to the boundaries of the computational domain are applied for the wind-driven case.

For the tidal case, a spatially uniform east-west velocity is applied at the eastern and western ends of the computational domain, and a condition of no flow normal to the boundaries is applied at the northern and southern boundaries of the domain. The computations indicate that wind-driven currents are small in comparison with tidal currents and that wind-driven currents are concentrated near the crest of the shoal. The computations indicate that tidal currents are deflected slightly around the shoal and they are intensified, relative to the ambient tidal current, over the shoal. Results from the wind-driven current model were also formatted for input to the sediment transport modeling (Section 2.3).

3.3 Sediment Transport Modeling

Analytical sediment transport modeling was performed to determine the extent to which existing wave and current conditions are likely to lift and move sand at the alternative wind farm sites. A comprehensive two-dimensional sediment transport model has been developed by Woods Hole Group, Inc. (WHG) based on theory and work conducted by Madsen and Grant (1976, 1977, 1978, 1986). WHG has coded the model to a computational format useful for applied coastal sciences and engineering projects, and previously applied the model successfully for similar studies (e.g., Jachec and Bosma, 2001). More details regarding the model theory are provided in Appendix C. The success of the model has been verified through comparison with historic net sediment transport rates in offshore areas in previous investigations (Applied Coastal Research and Engineering et al., 2000).

The model allows for characterization of sediment transport processes in response to wave-induced bottom currents, as well as ambient tidal and/or wind-driven currents. Model inputs include a grid of wave heights and ambient currents for a selected area of interest (in this case the three alternative wind farm sites). The model then calculates

near bottom velocities and shear stresses associated with waves and ambient currents, which provide the basis for the sediment transport calculations. Model output includes representation of whether and where sediment transport is likely to occur (i.e., is sediment movement initiated), as well as potential rates of bed load and suspended load sediment transport.

Prior to running the sediment transport model, appropriate wave and current conditions were selected as input. A total of 26 sediment transport modeling scenarios were simulated, including 8 combinations of waves and currents at each of the three sites. The 8 scenarios for each site consisted of:

- Mean ebb/flood currents with the most common waves (2);
- Spring ebb/flood currents with the largest waves (2);
- Spring ebb/flood currents with the largest waves in the same direction as the tidal currents (2); and
- Spring ebb/flood currents with the ocean waves (2).

Two additional simulations were examined for the Horseshoe Shoal that simulated the effects of wind-driven currents. Table 3-3 summarizes the sediment transport modeling simulations. The conditions were selected to represent the range of tidal currents, locally-generated wind waves within the Sound, ocean waves, and wind-generated wind-driven currents in the Sound. Not all of the wave and current combinations were modeled. Extreme conditions, such as storms, were not modeled.

The wave-induced bottom velocities are calculated based on linear wave theory that predicts the reduction in wave-induced current velocity with depth for a given surface wave height and period. Although the wave velocity is orbital (i.e., back and forth under the passing wave crest), it provides an important forcing function to lift sediments (i.e., sediment transport initiation). The near bottom tidal currents are calculated by the sediment transport model using a bottom boundary layer theory that predicts the decrease in currents with depth. The near bottom tidal current velocities can force a net transport of sediment in a particular direction if the combined wave-current velocities are sufficient to initiate sediment transport. The potential for sediment transport initiation is a qualitative measure that identifies areas most likely to experience sediment movement for a given condition. Finally, the potential net sediment transport rate quantifies the volumes of sediment that may be moved within a given time period, provided there is a sufficient sediment supply. The potential transport rate is given as cubic meters per meter per day (m^3/m/day). As such total volumetric rates along a cross-section of the area can be determined by simply multiplying the rate by a distance of interest.

Output for each sediment transport model simulation is illustrated by six plots, an example of which is shown by Figure 3-14 for the case at Horseshoe Shoal with mean flood currents and most commonly occurring waves in the Sound. The upper left plot shows wave-induced bottom velocities for the average wind speed from the most common direction (e.g., condition H11 from Table 3-2), which reach a maximum of approximately 0.1 m/s in a NE/SW direction. The upper right plot shows near-bottom

Table 3-3. Sediment Transport Modeling Simulations

Simulation	Tidal Currents	Sound Waves	Ocean Waves	Wind-driven Currents
Horseshoe Shoal				
	Mean Flood	H=1.3ft, T=2.3sec (H11)	-	-
	Mean Ebb	H=1.3 ft, T=2.3 sec (H11)	-	-
	Spring Flood	H=3.4 ft, T=3.6 sec (H6)	-	-
	Spring Ebb	H=3.4 ft, T=3.6 sec (H6)	-	-
	Spring Flood	H=3.4 ft, T=3.6 sec (H6)	-	-
	Spring Ebb	H=3.4 ft, T=3.6 sec (H6)	-	-
	Spring Flood		H=4.5ft; T=8sec	-
	Spring Ebb		H=4.5ft; T=8sec	-
	Spring Flood	H=3.4 ft, T=3.6 sec (H6)	-	Residual for 15 knot west wind
	Spring Ebb	H=3.4 ft, T=3.6 sec (H6)	-	Residual for 15 knot west wind
Tuckernuck Shoal				
	Mean Flood	H=1 ft, T=2 sec (T11)		-
	Mean Ebb	H=1 ft, T=2 sec (T11)		-
	Spring Flood	H=3.6ft, T=3.8 sec (T2)		-
	Spring Ebb	H=3.6ft, T=3.8 sec (T2)		-
	Spring Flood	H=3.3ft, T=3.5 sec (T14)		-
	Spring Ebb	H=3.3ft, T=3.5 sec (T14)		-
	Spring Flood		H=4.5ft; T=8sec	-
	Spring Ebb		H=4.5ft; T=8sec	-
Handkerchief Shoal				-
	Mean Flood	H=1.8ft, T=2.6 sec (M11)		-
	Mean Ebb	H=1.8ft, T=2.6 sec (M11)		-
	Spring Flood	H=3.4ft, T=3.7 sec (M12)		-
	Spring Ebb	H=3.4ft, T=3.7 sec (M12)		-
	Spring Flood	H=3.3ft, T=3.6 sec (M13)		-
	Spring Ebb	H=3.3ft, T-3.6 sec (M13)		-
	Spring Flood		H=4.5ft; T=8sec	-
	Spring Ebb		H=4.5ft; T=8sec	-

currents corresponding to the mean flood tide condition, which are between 0.4 and 0.6 m/s in an easterly direction. The middle left plot shows the relative potential for initiation of sediment transport for these combined wave and current conditions. The highest potential for sediment transport is along the shallow portions of the shoal on the northwest corner. There is little potential for sediment transport along the deeper portions of the shoal, particularly on the east side. The middle right plot shows a variable potential net rate of sediment transport. Maximum rates, even in the shallowest portions of the shoal, where the highest rates are expected and are more complex to model, are reasonable on the order of 3 m^3/m/day. This sediment transport rate can be interpreted as a few sand grains moving at an average speed of 1 cm/sec. There is near zero transport along the deeper portions of the shoal for this case. Finally, the bottom two plots of Figure 14 illustrate how the total net sediment transport rate is divided between suspended load (lower left) and bed load (lower right) transport. Bed load transport is much greater (order of magnitude) than suspended load transport. This is expected at the Horseshoe Shoal site, where sediments are relatively coarse, and are less likely to remain suspended in the water column. It is also an expected result for these relatively typical conditions where the level of wave and current turbulent energy is not sufficient to lift and suspend large volumes and concentrations of sediment within the water column.

Other sample plots of the sediment transport model results are shown by Figures 3-15 through 3-16. Figures 3-15 and 3-16 illustrate model results for Tuckernuck and Handkerchief Shoals also for the mean flood tide and typical wave conditions. By comparison, Handkerchief Shoal exhibits the most dynamic sediment transport conditions, which is expected due to the extensive shallow flats, relatively swift tidal currents that funnel at this location between the Sound and the Ocean, open western exposure to wave generated within the Sound, and relatively fine sediment grain size. Although Tuckernuck Shoal experiences the lowest tidal currents (Figure 3-9), the potential sediment transport rate for typical conditions is on the order of Horseshoe Shoal due to the fine sediment grain size at Tuckernuck Shoal. The highest transport rates along Tuckernuck Shoal are isolated to the localized shallow areas on the crest of the Shoal.

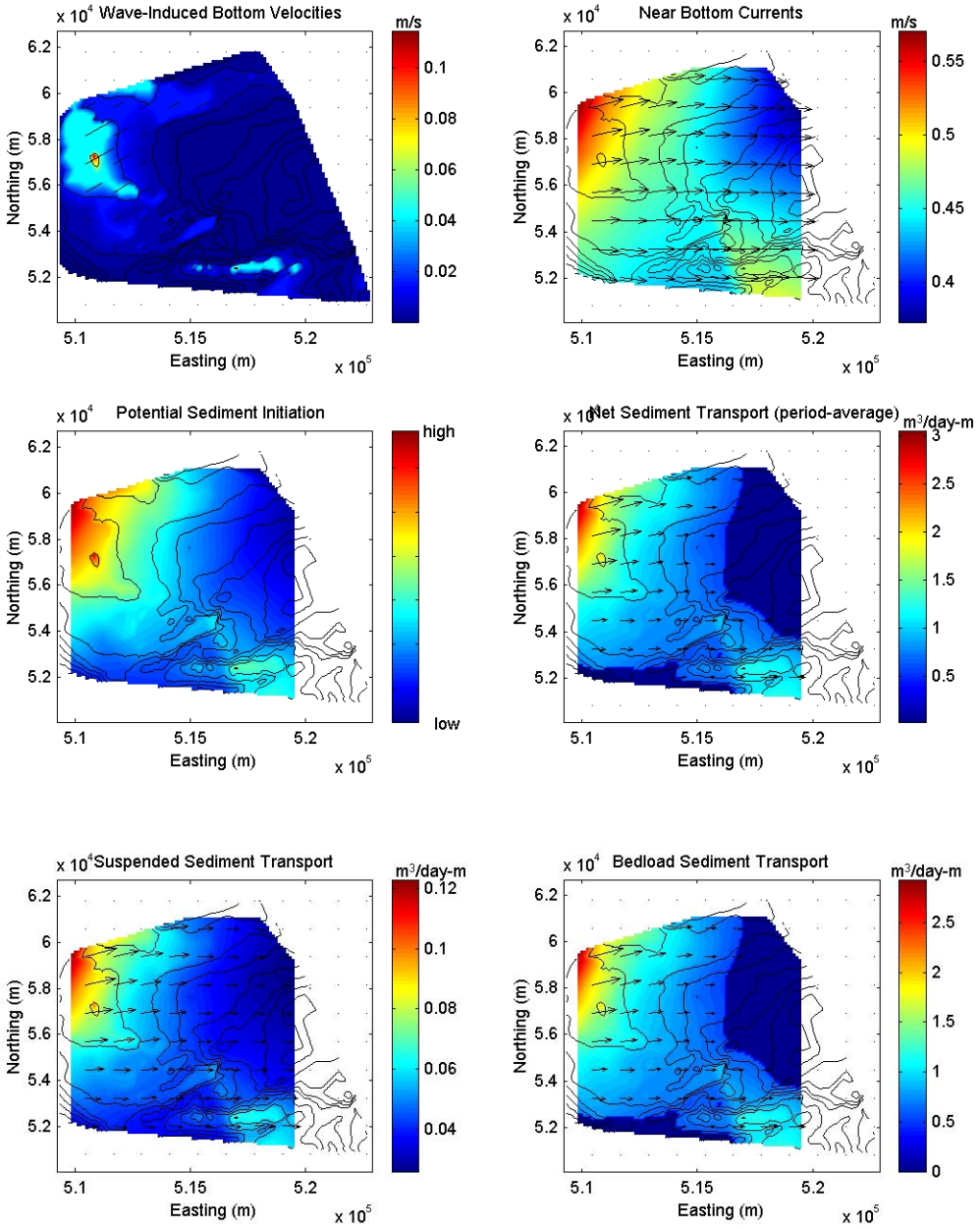

Figure 3-14. Sediment transport model results at Horseshoe Shoal for condition H-11 corresponding to mean flood tide conditions with commonly occurring waves

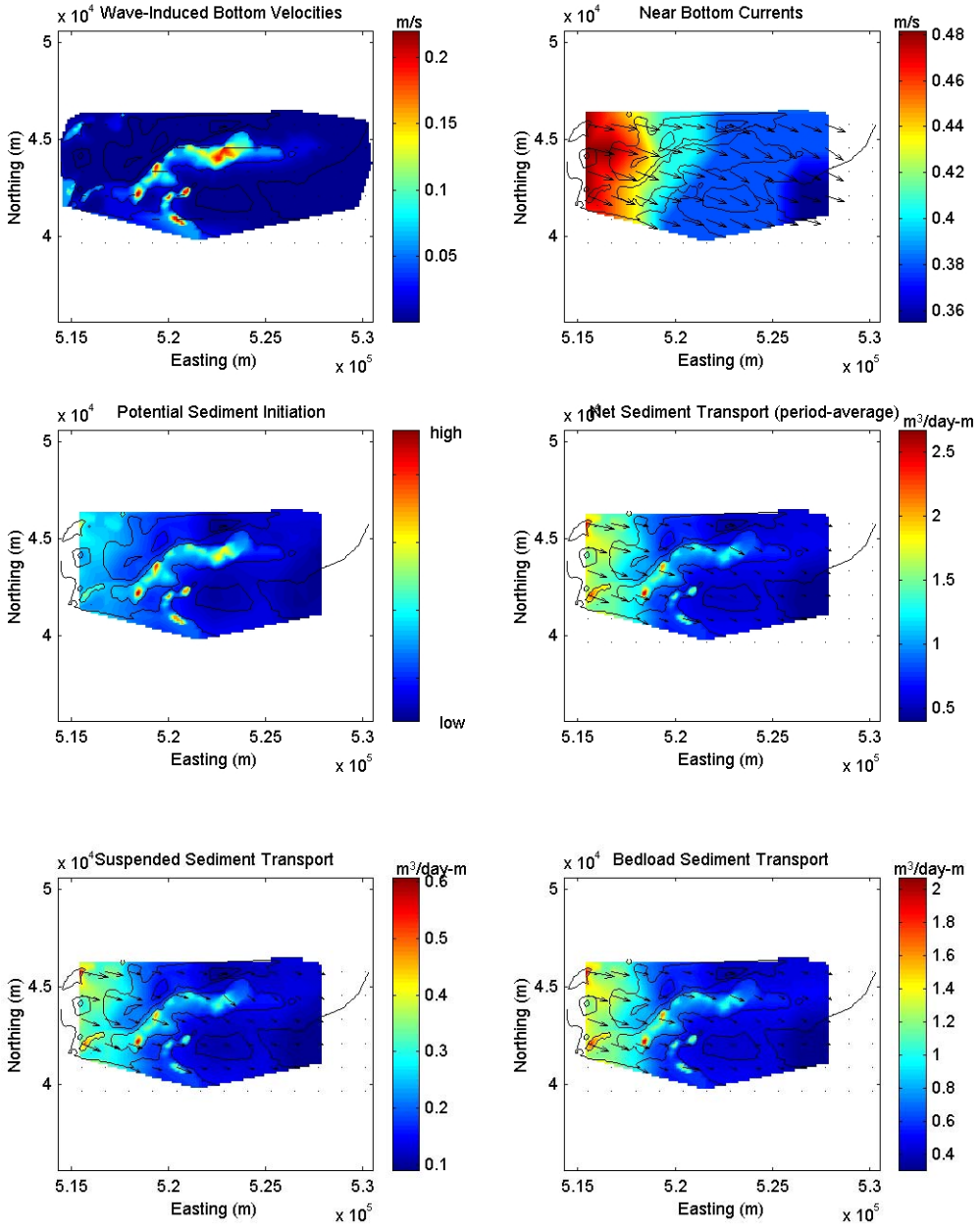

Figure 3-15. Sediment transport model results at Tuckernuck Shoal for condition T-11 corresponding to mean flood tide conditions with commonly occurring waves

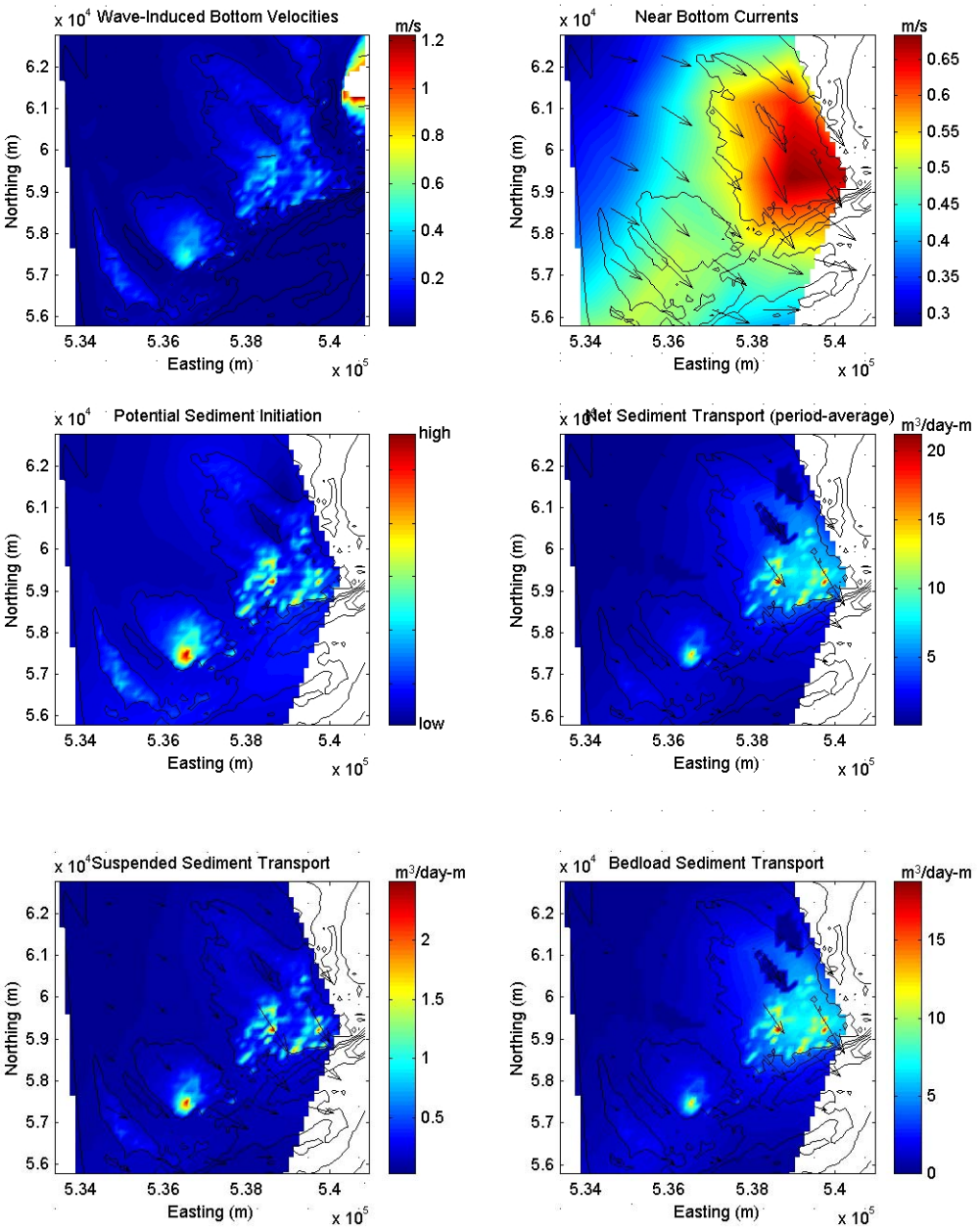

Figure 3-16. Sediment transport model results at Handkerchief Shoal for condition M-11 corresponding to mean flood tide conditions with commonly occurring waves

A complete set of sediment transport model output is contained electronically in Attachment A. General conclusions that can be drawn from the sediment transport modeling include:

- Since the flood tidal currents are stronger than ebb currents, there is a long-term forcing mechanism to cause the net transport of sediment to the east, particularly at Horseshoe Shoal.
- Locally-generated wind waves corresponding to the highest one-tenth wind speeds initiate significantly more sediment transport (e.g., ten times more) than waves corresponding to the average wind conditions in the Sound.
- Wind-driven currents can have a detectable affect on sediment transport rates, on the order of 20 percent of the ambient tidal currents for sustained westerly wind speeds of 15 knots. This conclusion is based upon sediment transport model simulations at Horseshoe Shoal, incorporating the wind-driven currents discussed in Section 3.2.2 and Appendix B. Table 3-3 defines the conditions that were simulated with the sediment transport model.
- If ocean swell waves are able to propagate to the site(s), the longer period associated with these waves can induce significant sediment transport (e.g., two orders of magnitude or 100 times more transport as compared to typical waves generated within the Sound). This conclusion is based on sediment transport modeling simulations at each of the three sites, incorporating the ocean wave conditions shown on Table 3-3.

These values for net, bed, and suspended sediment transport rates are useful for comparison purposes between various current and wave conditions, and to determine order of magnitude volumetric transport rates. The rates also can be applied to characterize morphologic changes, such as shoal migration, scour, or sediment infilling rates. Absolute values of sediment movement are not defensible from this analysis, though, without field measurements to verify model results. The model also does not account for erosion or equilibration of the seafloor. As such, the rates predicted by the model, particularly in the most shallow portions of the shoals, are likely overstated.

4.0 Summary And Conclusions

4.0 SUMMARY AND CONCLUSIONS

This report provides a characterization of existing current, wave, and sediment transport conditions at three locations within Nantucket Sound that were identified as alternative sites for the proposed wind farm. The characterization was developed based on compilation and analysis of existing data, collection of new current data, and application of analytical modeling techniques. The result provides an excellent source of background information and data related to existing conditions at the sites. The information can be used to assist with site selection, as well as to help determine the scope of environmental impact assessments.

4.1 Summary of Data

Existing data that were compiled included:

- Winds – Hourly measurements from Otis Airport between the late 1940's to present, Hyannis Airport (1973-2001), and Nantucket Airport (1986-2001).
- Bathymetry – Bottom depth measurements throughout Nantucket Sound from NOAA, and from ESS.
- Grain Size – Sediment grain size information was gathered from the USGS.
- Ocean Waves – Hindcast wave information from a 40-year period offshore Nantucket Island and Marthas Vineyard within the Atlantic Ocean.
- Tidal Currents – Tidal current information and observations within Nantucket Sound from a variety of sources dating back to the 1840s.
- Other data – Other data sets were identified but not included in this investigation, including offshore wave buoy measurements in the Atlantic Ocean and within Buzzards Bay, sediment core logs, side scan sonar data, and sub-bottom survey data.

New data collected included detailed current measurements within Nantucket Sound, specifically at various locations around Horseshoe Shoal, Tuckernuck Shoal, and Handkerchief Shoal. Measurements were collected using a vessel-mounted ADCP, and included current speed and direction at half-meter water depth increments throughout a tidal cycle (approximately 12 hours).

4.2 Summary of Modeling

Using the existing and new data, analytical models were applied to characterize wave, current (tidal and wind-driven), and sediment transport processes at the three alternative sites.

An analytical model developed by the USACE was used to model locally-generated wind waves in Nantucket Sound based on input wind information from Nantucket Airport. Ninety-six wave model simulations were conducted corresponding to various wind directions and speeds, although extreme conditions were not simulated. Locally-generated waves (significant wave height of the spectrum) within the Sound generally range from less than one ft to nearly four ft in height, with relatively short wave periods

(spectral peak) of less than 4 seconds. It should be noted that individual wave heights can be larger within the same spectrum. Once the wind-generated wave conditions were developed for each site, a shoaling calculation then was applied to characterize the spatial-distribution of wave height over each of the three shoals of interest.

In addition to locally-generated wind waves, swell waves from the Ocean were considered. Although previous literature suggests that ocean waves do not propagate to the nearshore area of Cape Cod, the data set was limited. As such, one average swell condition representative of waves from the east (H=4.5ft; T=8sec) was modeled approaching the Sound from the Atlantic Ocean between Monomoy Island and Nantucket Island. Conservative assumptions were incorporated that likely overstate the wave height at the shoals, because more sophisticated numerical wave modeling would be required to improve the accuracy. Nonetheless, the simplified swell analysis was performed to determine the relative potential effect on sediment transport. Measurements from the met-ocean tower will be valuable to determine whether swell waves from the Ocean impact the Horseshoe Shoal site.

Tidal currents were modeled based upon historical observations and new measurements at each of the three alternative sites. Current fields were developed for each site corresponding to mean flood and ebb currents, as well as spring flood and ebb currents. Flood currents are generally directed in an easterly direction, and ebb currents are generally directed westerly. Local changes in tidal current direction also occur on the shoals due to the nearby shoreline shape (e.g., the direction of tidal currents at Handkerchief Shoal is directed around Monomoy Island and have more of a southeast (flood)/northwest (ebb) sense), and due to bathymetric features (e.g., currents are diverted slightly around the shallowest portion of Horseshoe Shoal). Flood currents also are generally stronger than ebb currents, and spring tidal currents are approximately 20 percent stronger than mean tidal currents.

Wind-driven currents also were modeled because sustained winds within a semi-enclosed basin, such as Nantucket Sound, can induce currents in addition to ambient tidal currents. Because it was not possible to extract wind-driven current characteristics from the data, an analytical model was developed to simulate wind-driven currents at the Horseshoe Shoal site. Wind-driven current speeds were variable and strongest over the crest of the shoal, or approximately 15-20 percent of the tidal current speeds. As such, the effect of wind-driven currents on sediment transport also was evaluated.

Once the wave and current characteristics were evaluated, sediment transport calculations were made. An analytical sediment transport model was applied based on well-established theory from the published literature. The sediment transport model included calculations of wave-induced bottom current velocities, near-bottom tidal current velocities, a qualitative representation of where and whether sediment transport is likely to occur, and quantitative estimates of potential bed load, suspended load, and total sediment transport rates. The quantitative estimates of sediment transport rate are valuable for comparison purposes and for order of magnitude approximations, but are not defensible quantities without field measurements for verification. A total of twenty-six

sediment transport simulations were performed to evaluate a range of current and wave conditions at each site. It was generally found that active sediment transport occurs at all of the shoals, even under typical wave and tidal current conditions. The highest sediment transport rates are focused locally on the shallowest portions of the shoals, and there is relatively little sediment transport in the deeper regions for typical conditions. Bed load transport is typically an order of magnitude greater than suspended load transport. Spring tidal currents initiate approximately 20 percent more transport than mean tidal currents, and wind-driven currents from a typical 15 to 20 mph wind have a similar effect by comparison. The greatest impact on sediment transport initiation is due to waves. Larger locally-generated waves within the Sound can cause a significant increase in sediment transport. If swell waves from the Ocean impact the sites, sediment transport rates can increase as much as one-hundred fold, even for typical swell propagating from the Atlantic Ocean (e.g., 4.5 ft height with an 8 second period). Examples of sediment transport modeling results are presented.

5.0 References

5.0 REFERENCES

Applied Coastal Research and Engineering, Inc., Aubrey Consulting, Inc., Barry A. Vittor and Associates, Inc. and Continental Shelf Associates, Inc. 2000. "Environmental Survey of Potential Sand Resource Sites: Offshore New Jersey, Final Report." Prepared for the Minerals Management Service (INTERMAR) under contract number 14-35-01-97-CT-30864.

Bakker, W. T. 1974. "Sand Concentration in Oscillatory Flow." Proceedings of the 14th International Coastal Engineering Conference, ASCE, New York, pp. 1129-1148.

Bakker, W. T. and Th. Van Doorn. 1978. "Near-bottom Velocities in Waves with a Current." Proceedings of the 16th International Coastal Engineering Conference, ASCE, New York, pp. 1394-1413.

Chart Navigator 2002, v.5.0. Maptech Inc., Amesbury, MA, 2002.

Fredsoe, J. and R. Deigaard. 1992. *Mechanics of Coastal Sediment Transport.* Wold Scientific, New Jersey.

Goud, M. R. and D. G. Aubrey. 1985. "Theoretical and Observational Estimates of Nearshore Bedload Transport Rates." *Marine Geology*, vol 64, 91-111.

Grant, W. D. and O. S. Madsen. 1979. "Combined Wave and Current Interaction with a Rough Bottom." *Journal of Geophysical Research*, vol 84 (C4), 1797-1808.

Grant, W. D. and O. S. Madsen. 1986. "The Continental Shelf Bottom Boundary Layer." *Annual Review of Fluid Mechanics*, vol 18, 265-305.

Haight F. J. 1938. *Currents in Narragansett Bay, Buzzards Bay, and Nantucket and Vineyard Sounds.* U.S Department of Commerce, Special publication No. 208, Washington.

Jachec, S. M. and K. F. Bosma. 2001. "Sediment Transport Related to Potential Sand Mining Offshore New Jersey." *Ocean Wave Measurement and Analysis* (Editors: B. L. Edge and J. M. Hemsley) from Proceedings of the 4th International Symposium Waves 2001, ASCE. pp.1326-1335.

Jonsson, I. G. 1966. "Wave Boundary Layers and Friction Factors." *Proceeding of the 10th Conference on Coastal Engineering, ASCE*, vol 1, 127-148.

Jonsson, I. G. 1980. "A New Approach to Oscillatory Rough Turbulent Boundary Layers." *Ocean Engineering*, vol7, 109-152.

Kajiura, K. 1964. "On the Bottom Friction in an Oscillatory Current." *Bulletin of Earthquake Research, Inst. Tokyo University*, vol 42 (99), 147-174.

Kajiura, K. 1968. "A Model for the Bottom Boundary Layer in Water Waves." *Bulletin of Earthquake Research, Inst. Tokyo University*, vol 46, 75-123.

Kamphuis, J. W. 1975. "Friction Under Oscillatory Waves." *Journal of Waterways and Harbors, Coastal Engineering Division, ASCE*, vol 101, 135-144.

Knight, D. W. 1978. "Review of Oscillatory Boundary Layer Flow." *Journal of the Hydraulics Division, ASCE*, vol 104 (HY6), 839-855.

Madsen O. S. and W. D. Grant. 1976. *Sediment Transport in the Coastal Environment.* Report No. 209, MIT, Dept. of Civil Engineering, Cambridge, MA. 105 pp.

Madsen O. S. and W. D. Grant. 1977. Quantitative Description of Sediment Transport by Waves. Proceedings 15th International Coastal Engineering Conference, ASCE, New York, NY, pp. 1093-1112.

Madsen, O. S. and W. D. Grant. 1978. "Bottom Friction Under Waves in the Presence of a Weak Current." NOAA Technical Report ERL-MESA-29, 150 pp.

Madsen, O.S. 1993. *Sediment Transport Outside the Surf Zone*. Unpublished Technical Report, U.S. Army Engineer Waterways Experiment Station, Vicksburg, MS.

O'Hara, Charles J. and Robert N. Oldale. 1987. Maps Showing Geology, Shallow Structure, and Bedford Morphology of Nantucket Sound, Massachusetts.

Pedlosky, J. 1979. *Geophysical Fluid Dynamics.* Springer.

Press, W. H., Flannery, B. P., Teukolsky, S. A., Vetterling, W. T. 1989. Numerical Recipes. The Art of Scientific Computing. Cambridge University Press, New York, NY, 702 pp.

Raudkivi, A. J. 1990. *Loose Boundary Hydraulics, 3rd Edition*. Pergamon Press, Oxford.

Redfield A.C. 1980. *The Tides of the Waters of New England and New York*. Wm. S. Sullwold Publishing, Taunton, MA.

Shields, I. A. 1936. "Application of Similarity Principles and Turbulent Research to Bed-Load Movement (in German)." *Mitteilunden der Preoss*. Versuchsanst. Fur Wasserbau and Schiffbau, Berlin, No. 26.

Smith, J. D. 1977. "Modeling of Sediment Transport on Continental Shelves." *The Sea*, vol 6. Edited by Goldberg, McCave, O'Brien, and Steele. Wiley-Interscience, New York, NY.

Smith, J.D. and S.R. McLean. 1977. Spatially Averaged Flow over a Wavy Surface. *Journal of Geophysical Research*, Vol. 82, No. 12, 1735-1745.

Tanaka, H. and N. Shuto. 1981. "Friction Coefficient for a Wave-Current Coexisting System." *Coastal Engineering of Japan*, vol 24, pp. 105-128.

Trowbridge, J. and O. Madsen. 1984. "Turbulent Wave Boundary Layers, 1. Model Formulation and First-Order Solution." *Journal of Geophysical Research*, vol 89, 7989-7997.

Trowbridge, J. and V. C. Agrawal. 1995. "Glimpses of a Wave Boundary Layer." *Journal of Geophysical Research*, vol 100, 729-744.

U.S. Army Corps of Engineers. 1984. *Shore Protection Manual*. Dept. of the Army. Washington, DC.

U.S. Army Corps of Engineers. 1992. *Automated Coastal Engineering System (Wind Speed Adjustment and Wave Growth), Users Guide, Technical Reference*. Dept. of the Army, Vicksburg, MS.

Appendix A

Electronic Data and Model Results - CD

Appendix B

Wind-Driven Currents Theoretical Development

Notes on Wind-driven and Tidal Flow over Topography

John Trowbridge

June 10, 2002

1 Formulation

Consider small-amplitude, barotropic flow driven by winds or tides over variable bathymetry with scales small in comparison with the tidal wavelength. The linearized, depth-integrated, continuity equation with a rigid lid is

$$\frac{\partial}{\partial x}(hu) + \frac{\partial}{\partial y}(hv) = 0\,. \tag{1}$$

The linearized, depth-averaged, x-momentum equation is

$$\frac{\partial u}{\partial t} - fv = -\frac{1}{\rho}\frac{\partial p}{\partial x} + \frac{\tau_{wx}/\rho - ru}{h}\,, \tag{2}$$

and the linearized, depth-averaged, y-momentum equation is approximately

$$\frac{\partial v}{\partial t} + fu = -\frac{1}{\rho}\frac{\partial p}{\partial y} + \frac{\tau_{wy}/\rho - rv}{h}\,. \tag{3}$$

Here, t is time, x and y are horizontal coordinates, (u, v) is the depth-averaged horizontal velocity vector in the (x, y) system, $h(x, y)$ is the water depth, f is the Coriolis parameter, ρ is the constant density, p is the pressure, τ_{wx} and τ_{wy} are the x and y components of the wind stress, and r is a friction coefficient. For simplicity, the Coriolis parameter, wind stress, and friction coefficient are assumed constant.

To obtain a single equation describing the flow field, it is convenient to define a stream function, denoted $\psi(x, y)$, by

$$u = \frac{1}{h}\frac{\partial \psi}{\partial y}\,, \quad v = -\frac{1}{h}\frac{\partial \psi}{\partial x}\,, \tag{4}$$

and to eliminate p from (2) and (3):

$$\frac{\partial}{\partial t}\left(\frac{\partial v}{\partial x} - \frac{\partial u}{\partial y}\right) + f\left(\frac{\partial u}{\partial x} + \frac{\partial v}{\partial y}\right) = \frac{\partial}{\partial x}\left(\frac{\tau_{wy}/\rho - rv}{h}\right) - \frac{\partial}{\partial y}\left(\frac{\tau_{wx}/\rho - ru}{h}\right)\,. \tag{5}$$

The stream function satisfies (1) identically. Substitution of (4) into (5) gives

$$\frac{f}{h^2}\left(-\frac{\partial h}{\partial x}\frac{\partial \psi}{\partial y} + \frac{\partial h}{\partial y}\frac{\partial \psi}{\partial x}\right) = -\frac{\tau_{wy}}{\rho h^2}\frac{\partial h}{\partial x} + \frac{\tau_{wx}}{\rho h^2}\frac{\partial h}{\partial y} + \frac{rv}{h^2}\frac{\partial h}{\partial x} - \frac{ru}{h^2}\frac{\partial h}{\partial y} + \left(\frac{r}{h} - \frac{\partial}{\partial t}\right)\left(-\frac{\partial v}{\partial x} + \frac{\partial u}{\partial y}\right)\,, \tag{6}$$

or

$$\begin{aligned}\frac{f}{h^2}\left(-\frac{\partial h}{\partial x}\frac{\partial \psi}{\partial y} + \frac{\partial h}{\partial y}\frac{\partial \psi}{\partial x}\right) = &-\frac{\tau_{wy}}{\rho h^2}\frac{\partial h}{\partial x} + \frac{\tau_{wx}}{\rho h^2}\frac{\partial h}{\partial y} - \frac{r}{h^3}\frac{\partial h}{\partial x}\frac{\partial \psi}{\partial x} - \frac{r}{h^3}\frac{\partial h}{\partial y}\frac{\partial \psi}{\partial y} + \\ &\left(\frac{r}{h} - \frac{\partial}{\partial t}\right)\left(-\frac{1}{h^2}\frac{\partial h}{\partial x}\frac{\partial \psi}{\partial x} + \frac{1}{h}\frac{\partial^2 \psi}{\partial x^2} - \frac{1}{h^2}\frac{\partial h}{\partial y}\frac{\partial \psi}{\partial y} + \frac{1}{h}\frac{\partial^2 \psi}{\partial y^2}\right)\,,\end{aligned} \tag{7}$$

or

$$\frac{f}{h^2}\left(-\frac{\partial h}{\partial x}\frac{\partial \psi}{\partial y}+\frac{\partial h}{\partial y}\frac{\partial \psi}{\partial x}\right)=-\frac{\tau_{wy}}{\rho h^2}\frac{\partial h}{\partial x}+\frac{\tau_{wx}}{\rho h^2}\frac{\partial h}{\partial y}-\frac{2r-h\partial/\partial t}{h^3}\frac{\partial h}{\partial x}\frac{\partial \psi}{\partial x}-\frac{2r-h\partial/\partial t}{h^3}\frac{\partial h}{\partial y}\frac{\partial \psi}{\partial y}+\frac{r-h\partial/\partial t}{h^2}\nabla^2\psi\,. \tag{8}$$

In the frictionless, steady case, this expression reduces to the Taylor-Proudman theorem. In the case with constant depth and no planetary rotation, this expression reduces to the Laplace equation.

For simplicity, assume that the flow is time-periodic:

$$\psi(x,y,t)=\hat{\psi}(x,y)\exp(i\sigma t)\,, \tag{9}$$

where $\hat{\psi}(x,y)$ is complex and σ is the radian frequency. Then the equation determining ψ becomes

$$\nabla^2\psi-\frac{2r-i\omega h}{r-i\omega h}\frac{1}{h}\frac{\partial h}{\partial x}\frac{\partial \psi}{\partial x}-\frac{2r-i\omega h}{r-i\omega h}\frac{1}{h}\frac{\partial h}{\partial y}\frac{\partial \psi}{\partial y}+\frac{f}{r-i\omega h}\left(\frac{\partial h}{\partial x}\frac{\partial \psi}{\partial y}-\frac{\partial h}{\partial y}\frac{\partial \psi}{\partial x}\right)=\frac{\tau_{wy}/\rho}{r-i\omega h}\frac{\partial h}{\partial x}-\frac{\tau_{wx}/\rho}{r-i\omega h}\frac{\partial h}{\partial y}\,, \tag{10}$$

an elliptic equation that must be solved numerically in all but the simplest cases.

2 Finite-difference solution

Consider a problem with a rectangular domain. The origin is in the lower left corner of the domain. The x axis is positive to the right and the y axis is positive up. Discretize the domain into a regular array of grid points such that there are M grid points in the x direction and N grid points in the y direction. Number the grid points from $m=1$ to $m=MN$, with $m=1,2,...,M$ corresponding to the bottom row, $m=M+1,M+2,...,2M$ corresponding to the second row, and so on. Let the grid spacing in both the x and y directions be Δ. Grid point number m corresponds to row $=1+\text{floor}[(m-\epsilon)/M]$, where $0<\epsilon<1$, and column $=m-M(\text{row}-1)$. Grid point number m corresponds to $x=(\text{column}-1)\Delta$ and $y=(\text{row}-1)\Delta$.

Suppose that ψ is known on the boundaries of the domain. Rewrite the equation determining ψ as follows:

$$\nabla^2\psi+d(x,y)\frac{\partial \psi}{\partial x}+e(x,y)\frac{\partial \psi}{\partial y}=q(x,y)\,, \tag{11}$$

where

$$d(x,y)=-\frac{2r-i\omega h}{r-i\omega h}\frac{1}{h}\frac{\partial h}{\partial x}-\frac{f}{r-i\omega h}\frac{\partial h}{\partial y}\,,\quad e(x,y)=-\frac{2r-i\omega h}{r-i\omega h}\frac{1}{h}\frac{\partial h}{\partial y}+\frac{f}{r-i\omega h}\frac{\partial h}{\partial x}\,,\quad q(x,y)=\frac{\tau_{wy}/\rho}{r-i\omega h}\frac{\partial h}{\partial x}-\frac{\tau_{wx}/\rho}{r-i\omega h}\frac{\partial h}{\partial y}\,. \tag{12}$$

For interior points, the finite-difference approximation to this equation is

$$\frac{\psi_{m+1}-2\psi_m+\psi_{m-1}}{\Delta^2}+\frac{\psi_{m+M}-2\psi_m+\psi_{m-M}}{\Delta^2}+d_m\frac{\psi_{m+1}-\psi_{m-1}}{2\Delta}+e_m\frac{\psi_{m+M}-\psi_{m-M}}{2\Delta}=q_m\,, \tag{13}$$

or

$$\left(-\frac{1}{4}+\frac{\Delta e_m}{8}\right)\psi_{m-M}+\left(-\frac{1}{4}+\frac{\Delta d_m}{8}\right)\psi_{m-1}+\psi_m+ \tag{14}$$
$$\left(-\frac{1}{4}-\frac{\Delta d_m}{8}\right)\psi_{m+1}+\left(-\frac{1}{4}-\frac{\Delta e_m}{8}\right)\psi_{m+M}=-\frac{\Delta^2}{4}q_m\,,$$

where subscript m denotes evaluation at $[x(m), y(m)]$.

The solution requires that ψ be specified on the boundaries of the computational domain. The solution for ψ can be obtained by an iterative procedure in which one first guesses ψ (for example, by setting it equal to the boundary values) and then iterates for an updated solution for ψ_m by using (14).

3 Results

Results were obtained separately for wind-driven and tidal flows. In both computations, the model bathymetry is an elliptical shoal in a sea of constant depth. Although idealized, this bathymetry is qualitatively similar to the observed bathymetry over Horseshoe Shoal. The wind stress is $\tau_{wx} = 0.1$ N/m^2, corresponding to a wind speed of roughly 15 knots. The ambient tidal flow is 0.5 m/s. The linearized resistance coefficient is $r = 10^{-3}$ m/s, a relatively large value, reflecting the existence of strong tidal currents which enhance the bottom friction. The Coriolis parameter is 10^{-4} s^{-1} and the radian frequency of the tide is $\omega = 1.4 \times 10^{-4}$ s^{-1}, appropriate for the semi-diurnal tide. In the computation of the wind-driven flow, the boundaries of the computational domain is assumed to have no flow across them; i.e., the basin is assumed to be closed. This assumption, while reasonable, is clearly an idealization, because the boundaries of the real system shallow but not closed. The computation for the tidal flow imposes a known flow across the eastward and westward boundaries of the computational domain.

The results indicate a wind-driven flow (Figure 1) that is weak because of the strong friction and the assumption of a closed basin. The flow is downwind at the crest of the shoal and there is a weak return flow at larger depths. The flow turns slightly to the right over the crest of the shoal because of the earth's rotation. Although crude, the results clearly indicate that the wind-driven flow is small in comparison to the tidal flow.

The results indicate a tidal flow (Figure 2) that accelerates over the shoal in order to satisfy the continuity equation. The computation indicates little veering of the tidal current around the shoal. The computation indicates that the tidal current is enhanced near the crest of the shoal by a factor of about 1.6.

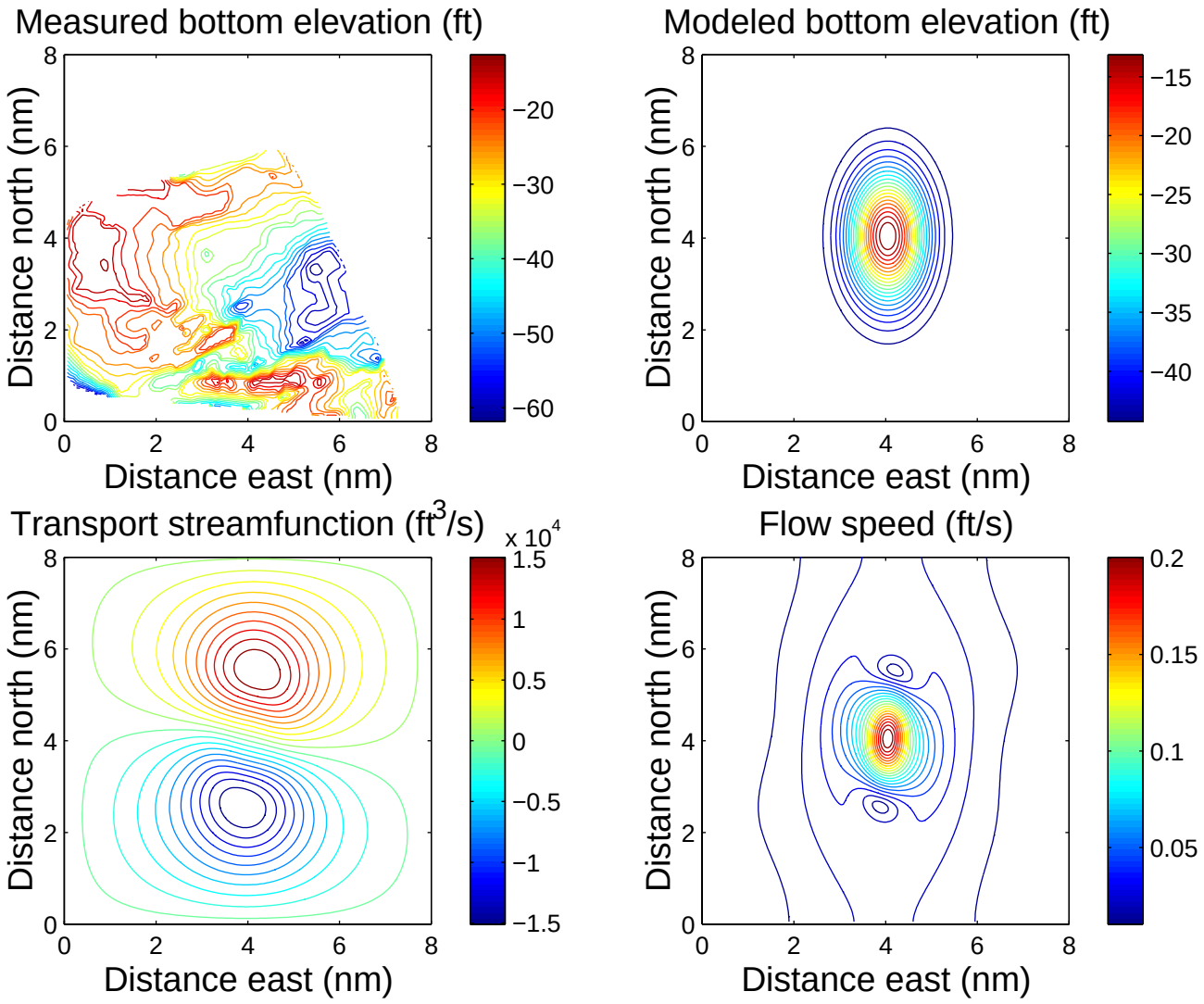

Figure 1: Model calculations of wind-driven flow.

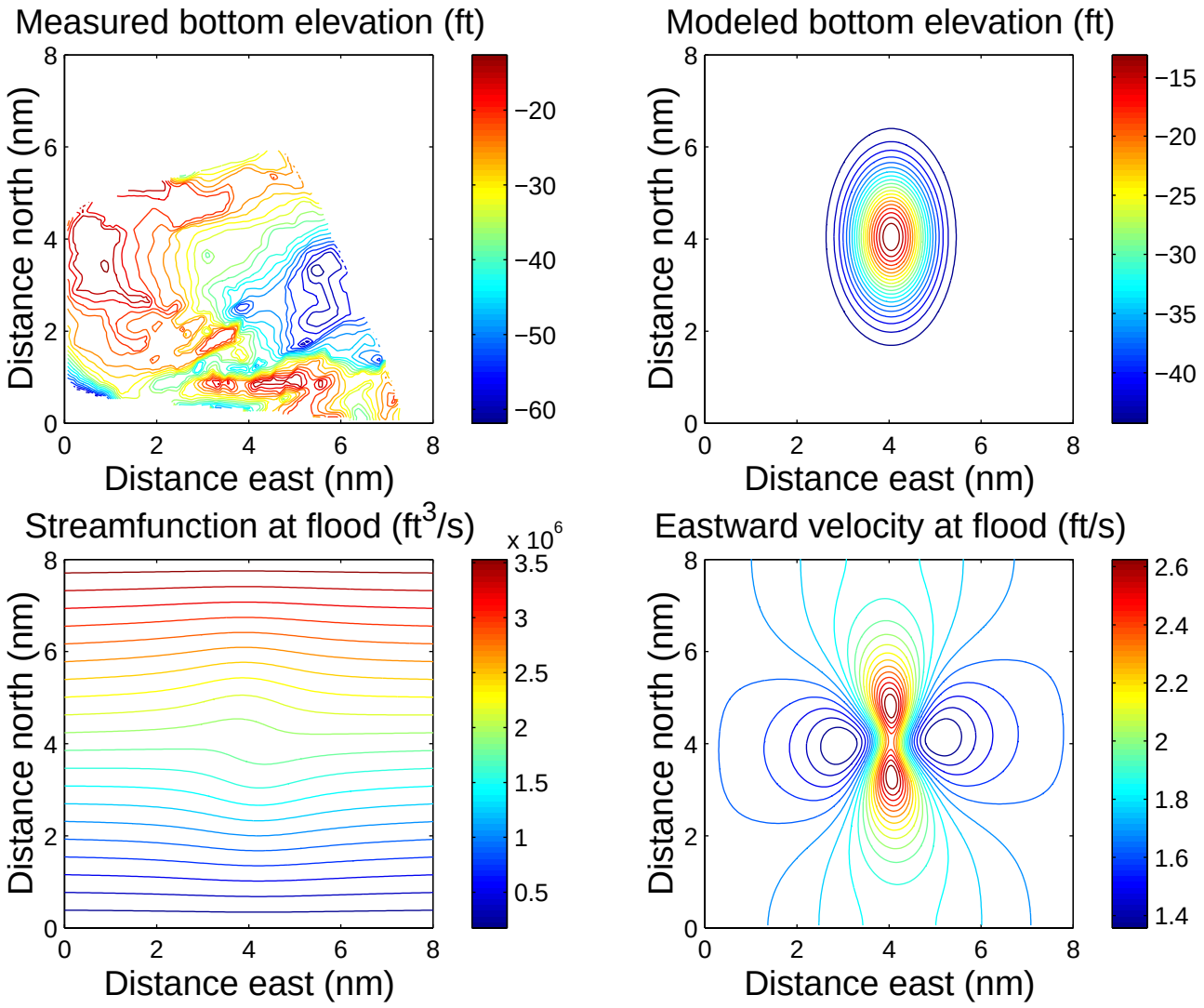

Figure 2: Model calculations of tidal flow.

Appendix C

Sediment Transport Model Theory

APPENDIX C SEDIMENT TRANSPORT MODEL THEORY

C.1 Wave-Induced Bottom Currents

A propagating wave not only causes a displacement in the water surface, but also displaces water particles beneath the passing wave. This displacement induces local currents, which over the period of the passing wave take on an orbital shape (orbital velocities). In shallow water, the orbits of water particles tend to take on an elliptical shape, while in deeper water the orbits are more circular (Figure C.1). Associated with these water particle trajectories are the particle horizontal (u_{orbit}) and vertical (w_{orbit}) orbital velocity components. These velocity components contribute to the initiation and transport of sediment at the bed. Therefore, knowledge of orbital velocities at the seabed is key in determining sediment transport characteristics at potential borrow areas. This section describes the method used to calculate wave-induced orbital velocities at the seabed.

Figure C.1. Shallow water and deep water wave orbits.

The relationship between a progressive wave and the particle motion it generates beneath the surface is well described by linear wave theory. Linear wave theory is used to derive the expression of the velocity potential (ϕ) as:

$$\phi = -\frac{H g}{2\sigma}\frac{\cosh k\left(h+z\right)}{\cosh\left(k h\right)}\cos\left(k x\right)\sin\left(\sigma t\right) \qquad \text{(C.1)}$$

where H is the wave height; ϕ is the wave frequency; k is the wave number; h is the still water depth; z is the depth of interest in the water column (positive upwards from still water); x is the horizontal point of interest along the wave, g is the gravitational constant, and t is the temporal point of interest. The resulting horizontal and vertical velocities under the wave are given by:

$$u_{orbit} = \frac{-\partial\phi}{\partial x} = \frac{H}{2}\sigma\frac{\cosh k\left(h+z\right)}{\sinh\left(kh\right)}\cos\left(k x - \sigma t\right) \qquad \text{(C.2)}$$

$$w_{orbit} = \frac{-\partial \phi}{\partial z} = \frac{H}{2}\sigma \frac{\sinh k(h+z)}{\sinh(kh)} \sin(k x - \sigma t) \qquad \text{(C.3)}$$

Equations (C.2) and (C.3) reveal that the velocity at the bottom (z = -h) consists only of the u_{orbit} component, while w_{orbit} is zero. Thus, at the seabed, the motion of the water particles is purely horizontal (assuming the water cannot penetrate the seabed). This allows the reduction of the velocity at the bottom to:

$$U_B = \frac{H}{2} \frac{\sigma}{\sinh(k h)} \qquad \text{(C.4)}$$

The horizontal motion, as the seabed oscillates positively (under a crest) and negatively (under a trough), depends on the spatial and temporal position of the wave (Figure C.2). The absolute maximum bottom currents induced by the wave occur at the crest and/or the trough of the passing wave.

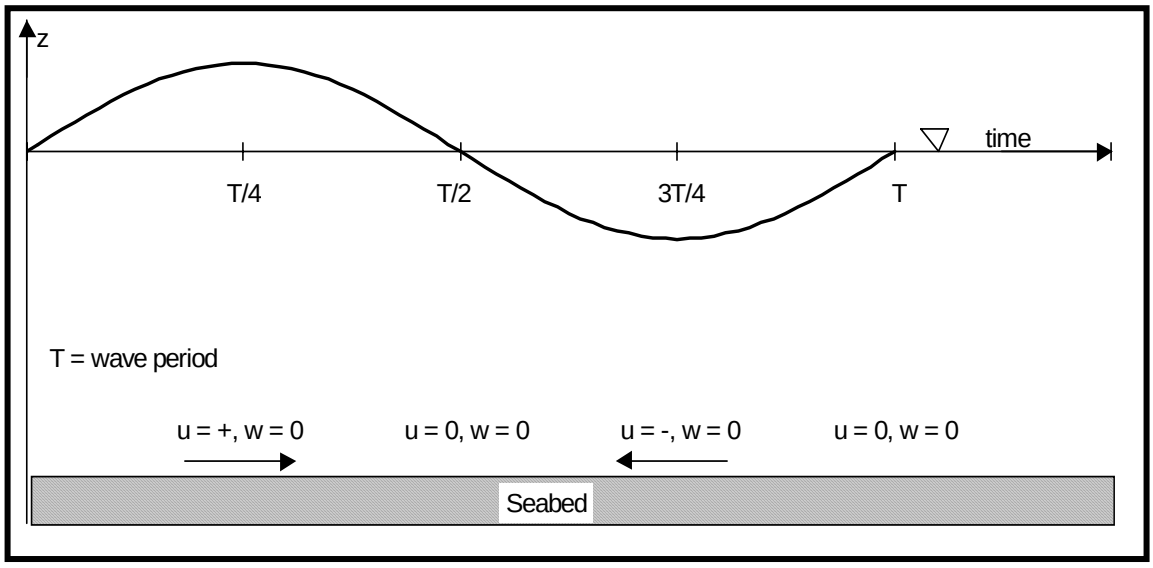

Figure C.2. Schematic of wave-induced bottom velocities.

Applying linear wave theory, coupled with the wave parameters at the dredged borrow area, wave-generated bottom currents can be determined. Wave height, wave period, wave direction, and water depth are used to calculate the maximum bottom horizontal orbital velocity at the seafloor for each grid point within the selected domain. Wave-induced bottom velocities can then be combined with tidally driven currents and utilized to determine sediment initiation and potential transport.

The wave-induced bottom velocity is a key factor contributing to the initiation and transport of sediment. Although for purely sinusoidal motion, no net sediment transport is caused by the wave orbital motions, shearing velocities created at the seabed by the waves are a primary contributor to the initialization of sediment into the water column (Fredsoe and Deigaard, 1992).

Assuming purely oscillatory wave motion (linear theory) without currents results in no net sediment transport. If sediment is lifted from a non-sloping seafloor into the water column, the amount of sediment transported forward (in the direction of wave propagation) during half of the cycle will equal the amount being transported backwards during the second half of the cycle. In order to cause a net difference in sediment transport, additional physical phenomena are required. These include:

- bottom slopes on the seafloor
- tidal and/or wind-driven currents
- wave asymmetry (non-linearity)
- wave-induced mass transport

C.2 Combined Wave Tidal and Current Bottom Boundary Layer

In areas outside the surfzone, it is critical to account for wave and current interactions within the bottom boundary layer when evaluating potential sediment transport. Even though introducing coastal and/or tidal currents to wave motions adds difficulty in estimating shear, dissipation, and sediment transport dynamics, it is critical to consider both physical mechanisms. A number of approaches have been developed by Lundgren (1972), Bakker (1974), Smith (1977), and Bakker and van Doorn (1978) to attempt to solve this problem.

Madsen and Grant (1976, 1977), Grant and Madsen (1978, 1979), and Tanaka and Shuto (1981) considered current and wave interaction situations, where the current and wave have an arbitrary angle with each other. Tanaka and Shuto used a one-layer eddy viscosity approach, which most likely over simplified the problem. Madsen and Grant (1976, 1977), and Grant and Madsen (1978, 1979) derived sediment transport relationships for predicting net sediment transport rates in the presence of second order effects such as bottom slope, wave asymmetry, coastal currents, and mass transport currents. They concluded that only cases involving small amplitude wave theory (i.e. linear) and a steady current are understood to a level that it is reasonable to evaluate resulting sediment transport rates with any degree of confidence. When taking representative phases of tidal flow, this approach can be applied to the alternative sites.

In this study, u_{cw} was used to represent the combined wave/current reference velocity and include effects of waves and a steady current. A combination of the two creates a realistic representation of maximum bottom velocity and bed shear stress (Figure C.3). Proper combination of wave-induced and ambient currents requires an accurate representation of flow dynamics located directly at the seabed. The combined wave/current reference velocity, u_{cw}, is a function of the wave-induced bottom orbital velocity (Equation C.4) and the apparent current velocity at the bottom, U_a, as given by:

$$\vec{u}_{cw} = \left(U_b \cos \omega t + U_a \cos \phi_a, U_a \sin \phi_a\right) \qquad \text{(C.5)}$$

where U_b = wave-induced bottom velocity
U_a = apparent ambient current bottom velocity
ϕ_a = the angle between the apparent current and wave-induced current (Figure C.3)

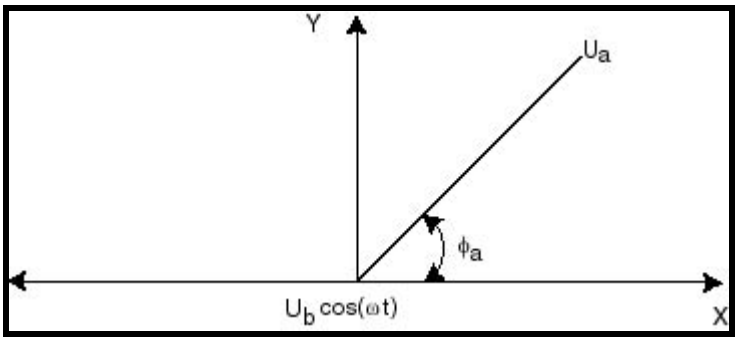

Figure C.3. Illustration indicating the angle between the apparent bottom current and wave-induced bottom current (Grant and Madsen, 1979).

In most cases, it is difficult to measure ambient current magnitude and direction directly at the seafloor. Because current observations were not measured directly at the bottom, they must be translated to the seafloor based on the application of a current profile through the bottom boundary layer. In order to determine the appropriate vertical current profile, the thickness of the bottom wave/current boundary layer (δ_w) must be determined and compared to the observed current location within the water column. A significant amount of work has been completed relative to the wave/current bottom boundary layer (Kajiura, 1964; Kajiura, 1968; Kamphuis, 1975; Knight, 1978; Bakker and van Doorn, 1978; Grant and Madsen, 1979; Trowbridge and Madsen, 1984). In addition, Trowbridge and Agrawal (1995) collected field data within the bottom boundary layer. Jonsson (1980) presents an equation for the thickness of the wave boundary layer in oscillatory rough turbulent flow, which is most common in nature, as:

$$\delta_w = \frac{2\kappa U_{*m}}{\omega} \qquad \text{(C.6)}$$

κ = Von Karman's constant (0.4)
U_{*m} = the maximum current velocity at the seabed
$\omega = 2\pi/T$

If observed currents were measured outside of the bottom boundary layer ($z > \delta_w$), which is usually the case in field measurements, a logarithmic current profile is assumed, as:

$$U_c = \frac{U_{*c}}{\kappa} \ln\left(\frac{30z}{k_{bc}}\right) \qquad \text{(C.7)}$$

where U_{*c} = the critical bottom velocity
z = height above the bed
U_c = the magnitude of the measured current
k_{bc} = the apparent bed roughness

The apparent bed roughness presented in Equation C.7 is defined as:

$$k_{bc} = k_b \left(60\kappa \frac{U_{*m}}{k_b \omega} \right)^{\beta} \quad \text{(C.8)}$$

where k_b is the roughness coefficient, which is assumed to be equivalent to d_{50} of the local sediment, and $\kappa = 1-(U_{*c}/U_{*m})$.

C.3 Initiation of Sediment Motion Under Combined Wave and Tidal Currents

Before sediment can be transported, it must be lifted from the seabed by combined wave and current motion. When sufficient stress is applied to the bed, sediment may begin to move. When subjected to a large enough flow, the driving forces impacting sediment grains exceed the stabilizing forces, and sediment will begin to move.

Through dimensional analysis, Shields (1936) derived an expression that identifies the point where bed stress equals bed resistance. The threshold of particle motion is based on a ratio between the driving forces (drag and lifting forces) and stabilizing forces (frictional forces) as seen in Figure C.4. The Shields parameter (ψ) results from equating the driving and stabilizing forces. For a flat bed:

$$\psi = \frac{\tau_b}{(s-1)\rho g\, d_{50}} \quad \text{(C.9)}$$

where τ_b = maximum bottom shear stress
ρ = density of the sea water
s = relative density (equals 2.65 for natural sediment)
g = acceleration due to gravity
d_{50} = grain diameter which corresponds to 50% by weight finer

The shear stress at the bed, τ_b, is given by Madsen and Grant (1976) and Raudkivi (1990) as:

$$\vec{\tau}_b = \frac{1}{2} \rho f_{cw} |\vec{u}_{cw}| \vec{u}_{cw} \quad \text{(C.10)}$$

where f_{cw} is the combined wave/current friction factor and u_{cw} is the combined wave/current reference velocity.

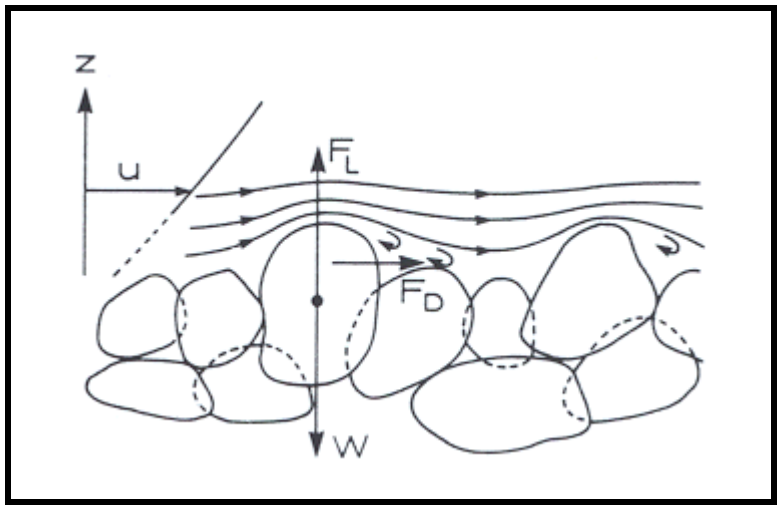

Figure C.4. Forces acting on grains resting on the seabed (Fredsoe and Deigaard, 1992). F_L = lifting force, F_D = drag force, and W = grain weight.

Having the combined wave and ambient current velocity at the bottom, the bottom shear stress resulting from combined wave/current interaction can be determined. Maximum bottom shear stress, $\tau_{b,max}$, due to the combined current and wave action can be determined from:

$$\tau_{b,\max} = \rho U_{*m}^2 = \frac{1}{2}\rho f_{cw} U_b^2 \left(1 + 2\varepsilon \cos\phi_a\right) \tag{C.11}$$

where $\varepsilon = (U_a/U_b)$.

The combined wave/current friction factor, f_{cw}, is provided by Madsen and Grant (1976) as:

$$f_{cw} = \frac{U_c f_c + U_b f_w}{U_c + U_b} \tag{C.12}$$

where f_c and f_w are friction factors corresponding to ambient current flow and wave-induced flow, respectively. The wave friction factor was presented by Jonsson (1966a) and is a function of the wave Reynolds number and (U_b/k_bT).

$$f_w = f_w\left(\frac{U_b^{\,2}}{\nu\omega}, \frac{U_b}{k_b\omega}\right) \tag{C.13}$$

The wave friction factor can be determined using Jonsson's wave friction factor diagram (Jonsson, 1966a). In a similar manner, the current friction factor can be determined from the standard Darcy-Weisbach approach:

$$f_c = \frac{1}{4} f\left(\frac{U_m 4h}{\nu}, \frac{d_{50}}{4h}\right) \tag{C.14}$$

The maximum bottom shear stress under the combined wave/current interaction is then used to calculate the Shields parameter (Ψ_{max}) from Equation 2.9, recast as:

$$\Psi_{max} = \frac{U_{*m}^2}{g(s-1)d_{50}} \tag{C.15}$$

Once the Shields parameter has been calculated at points of interest, the resulting values can be compared to a critical Shields parameter (Ψ_{crit}) to determine if sediment initiation occurs at each point of interest. The critical Shields parameter may be determined using a modified Shields diagram developed for sediment transport in the coastal environment (Madsen and Grant, 1976, 1977).

In addition, modifications have been made to the critical Shields parameter to account for sloped bed forms. If sand grains are placed on a bed with a transverse slope or longitudinal slope, it is either easier or more difficult to initiate movement based on the direction of current flow (Figure C.5). In the transverse case, the flow direction is perpendicular to the slope, while in the longitudinal case, the flow travels parallel to the slope. Therefore, sediment is initiated more easily on a downward slope than an upward slope and the critical Shields parameter decreases or increases according to bathymetry. Equations C.16 and C.17 take into account the transversely and longitudinally sloped bed forms, respectively, and provide an adjusted Ψ_{crit}:

$$\Psi_{crit} = \Psi_{\substack{critical\ for \\ a\ flat\ bed}} \cos\beta \sqrt{1 - \frac{\tan^2\beta}{\tan^2\phi_s}} \tag{C.16}$$

$$\Psi_{crit} = \Psi_{\substack{critical\ for \\ a\ flat\ bed}} \cos\gamma \left[1 - \frac{\tan\gamma}{\tan\phi_s}\right] \tag{C.17}$$

where β = transverse bed slope,
γ = longitudinal bed slope, and
ϕ_s = angle of repose

Finally, by comparing maximum and critical Shields parameters, sediment initiation can be determined at locations within and surrounding the offshore borrow areas. If ψ_{max} exceeds ψ_{crit}, sediment will move. At each point within the selected observation area, the Shields parameter was determined and compared to the critical Shields parameter at that same grid point to determine the likelihood of sediment transport.

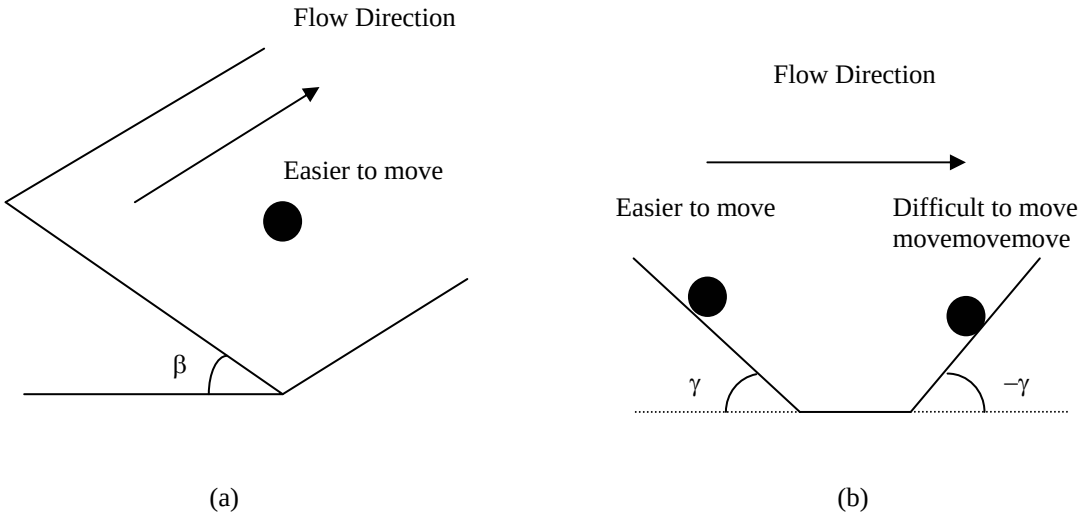

Figure C.5. Illustration of a particle on a (a) transverse slope, and on a (b) longitudinal slope.

C.4 Bed-Load Sediment Transport

Sediment initiation provides valuable insight into sediment movement, but does not provide information as to how much sediment moves and in what direction is it traveling. Therefore, sediment transport rates and transport directions need to be calculated in and around the offshore borrow area to assess overall sediment transport potential as well as provide insight into:

- approximate rates of sediment transport;
- seasonal patterns of sediment transport;
- influence of storm events on sediment transport;
- estimates on borrow site recovery times; and
- directional fluctuations in sediment transport patterns.

For Shields parameter values slightly above critical or, more specifically, for low transport rates, the predominant mode of sediment transport takes place as individual grains rolling, sliding, and/or jumping along the bed (e.g., saltation). This mode of sediment transport is referred to as bed-load, since it takes place in close proximity of the bed. The bed-load transport formulas applied here are based on analytical expressions developed by Madsen and Grant (1976). Qualitatively they involve:

- determining the time-varying values of sediment transport in the northing (y) and easting (x) directions;
- period-averaging these sediment transport component results; and
- calculating the net bed-load sediment transport magnitude and direction.

Determination of the instantaneous sediment transport rate is given by the following equations:

$$q(t)_{bedload,y} = 40\,\omega_{fall}\,d_{50}\left[\frac{\frac{1}{2}f_{cw}\left(u(t)^2+v(t)^2\right)}{(s-1)\,g\,d_{50}}\right]^3 * \frac{v(t)}{\sqrt{u(t)^2+v(t)^2}} \qquad \text{(C.18)}$$

$$q(t)_{bedload,x} = 40\,\omega_{fall}\,d_{50}\left[\frac{\frac{1}{2}f_{cw}\left(u(t)^2+v(t)^2\right)}{(s-1)\,g\,d_{50}}\right]^3 * \frac{u(t)}{\sqrt{u(t)^2+v(t)^2}} \qquad \text{(C.19)}$$

where $q(t)_{bedload,\,y}$ = bed-load sediment transport rate in northing direction
$q(t)_{bedload,\,x}$ = bed-load transport rate in easting direction
v(t) = time-dependent wave orbital bottom velocity and steady near bottom current in the northing direction
u(t) = time-dependent wave orbital bottom velocity and steady near bottom current in the easting direction
ω_{fall} = sediment fall velocity

To determine the net sediment transport rate per wave cycle, sediment transport rates were period-averaged. The net period-averaged sediment transport rates in the northing $\left(\bar{q}(x,y)_{bedload,y}\right)$ and easting $\left(\bar{q}(x,y)_{bedlaod,x}\right)$ directions, respectively, are:

$$\bar{q}(x,y)_{bedload,y} = \frac{1}{T}\int_0^T q(t)_y\,dt \qquad \text{(C.20)}$$

$$\bar{q}(x,y)_{bedload,x} = \frac{1}{T}\int_0^T q(t)_x\,dt \qquad \text{(C.21)}$$

The northing and easting components can be combined by determining the sediment transport magnitude $(\bar{q}(x,y))_{\text{bedload}}$ defined as:

$$\bar{q}(x,y)_{bedload} = \sqrt{\left[\bar{q}(x,y)_y\right]^2 + \left[\bar{q}(x,y)_x\right]^2} \qquad \text{(C.22)}$$

In addition to magnitude, the net direction can be calculated based on the bed-load sediment transport components. Results of the analyses were used to estimate the rate of sediment movement and the direction of transport, which are presented in Chapter 4.0.

C.5 Suspended-Load Sediment Transport

In low transport rate areas, or where sediment grains are large, the predominant mode of transport is bed-load. As flow intensity increases, or in the case of smaller grain sizes, individual grains may leave the bottom with increasing frequency and the mode of

transport may change from sediment particles rolling and sliding along the bottom, particles jumping and staying suspended in the water column. For this mode of transport, sediment is no longer in contact with the bed. Sediment transport associated with sediment making a series of jumps along the bottom, referred to as saltation, provides a transition from the bed-load transport discussed in the previous section to the suspended-load transport that takes place in the overlying water column.

Distribution of suspended-load in the water column is governed by the fall velocity of the sediment, w_f. In order to solve the equations governing the distribution of suspended sediment concentration throughout the water column, it is necessary to determine the fall velocity for each distinct sediment type. For natural, non-cohesive, granular sediments, the force balance of submerged weight and fluid drag on a grain falling through quiescent fluid is:

$$w_f = \sqrt{\frac{4}{3C_D}}\sqrt{(s-1)gD} \tag{C.23}$$

After determining the appropriate fall velocities for each node in the modeling domain, it was necessary to specify the boundary conditions for the suspended-load transport. One boundary condition is simply that no sediment is transported through the water surface. Madsen (1993) provides the most commonly accepted form of the bottom boundary condition, or specification of a reference concentration, as:

$$C_R = \gamma C_b \left(\frac{\left|\overline{\tau_b}\right|}{\tau_{cr}} - 1 \right) \tag{C.24}$$

where (is the so-called resuspension parameter and C_b is the volume concentration in the bed. Typically, C_b is taken as 0.65 (Smith and McLean, 1977) for a bed consisting of cohesionless sediment. The periodic component of the reference concentration (Madsen, 1993), or the wave reference concentration, is given by:

$$C_{RW} = \gamma C_b \left(\frac{4}{\pi} \frac{\tau_c}{\tau_{cr}} \cos\phi_{cw} - \frac{\tau_w}{\tau_{cr}} \frac{\tan\beta}{\tan\phi_m} \right) \cos\theta \tag{C.25}$$

where ϑ_c = current bottom shear stress
ϑ_w = maximum wave current bottom shear stress
$\exists$ = Bottom slope of bed
N_m = friction angle of sediment
cos 2 = temporal variation (phase component and angle)

Equation C.25 is time-averaged such that the temporal variation (phase component and angle) drops out of the equation.

Finally, the suspended-load transport is the product of suspended sediment concentrations and velocity, which is then integrated over depth and time-averaged. This includes components for both mean current and wave-associated suspended-loads. Both the mean current suspended-load transport and the mean wave-associated suspended-load transport must be determined for cases both inside and outside the wave/current boundary layer. Details of these rather complex and lengthy equations are presented in Madsen (1993).